

## Observations of the Hyades open cluster during the all-sky survey with the SRG/eROSITA telescope.

I. M. Khamitov<sup>\*1</sup>, I. F. Bikmaev<sup>1</sup>, M. R. Gilfanov<sup>2,3,1</sup>, R. A. Sunyaev<sup>2,3</sup>, P. S. Medvedev<sup>2</sup>, M. A. Gorbachev<sup>1</sup>, A. S. Sklyanov<sup>1</sup>, P. D. Efremova<sup>1</sup> and S. S. Panarin<sup>1</sup>

<sup>1</sup>Kazan Federal University, Kazan, Russia

<sup>2</sup>Space Research Institute of Russian Academy of Sciences, Moscow, Russia

<sup>3</sup>Max-Planck Institute for Astrophysics, Garching, Germany

Received January 30, 2026

**Abstract** — Using data from the *eROSITA* all-sky X-ray survey aboard the *SRG* orbital observatory and an optical catalog of members of the Hyades open cluster based on *Gaia* data, we investigated the coronal X-ray emission of the cluster's stars. Out of 395 known members located in the eastern Galactic hemisphere, *eROSITA* detects X-ray emission from 290 stars, including 171 sources identified in X-rays for the first time. At the distance of the Hyades ( $\sim 47$  pc), the median sensitivity of *eROSITA* in this region of the sky corresponds to a luminosity of  $L_X \sim 2.6 \times 10^{27}$  erg s $^{-1}$  in the 0.3–2.3 keV energy band, enabling the detection of 100% of cluster members of spectral types from F0 to K5 within the cluster's tidal radius. We also examined objects located in the Hyades tidal tails, where *eROSITA* detects X-ray emission from 114 out of 281 known members, 59 of which are newly identified X-ray sources.

Strong X-ray variability (by more than an order of magnitude) on a timescale of six months was observed for six sources, all of which are late-M-type binaries. The distribution of Hyades members over the ratio  $R_X = \log(L_X/L_{\text{bol}})$  shows a distinctly bimodal structure: the left peak at  $R_X \sim -4.7$  is formed mainly by FGK-type stars, while the right peak at  $R_X \sim -3.2$  consists mostly of M-type stars.

The dependence of  $R_X$  on the Rossby number ( $Ro$ ) differs for M-type and FGK-type stars. For M dwarfs,  $R_X \approx -3$  remains nearly constant at low  $Ro$  and declines sharply at  $Ro \gtrsim 0.2$ . In contrast, most F-, G-, and K-type stars occupy a relatively compact region at  $Ro \sim 0.3$ –0.8 and  $R_X \sim -4.7$ .

Key words: *X-ray sources; stars; open clusters: Hyades; instruments: SRG/eROSITA, ROSAT/PSPC*

### INTRODUCTION

The Hyades open cluster contains about 790 confirmed members (according to *Gaia* DR3, Žerjal et al. (2023)), with an estimated age of 640–720 Myr and a mean distance of 47 pc. A comprehensive review of age and distance determinations for the cluster is given by Lodieu et al. (2019).

Due to its proximity and the relatively high brightness of its members (some of which are visible to the naked eye), the Hyades cluster has long served as an important laboratory for studying the evolution of coronal activity in late-type stars. An additional advantage of studying open cluster members lies in their well-constrained ages and chemical compositions, in contrast to field stars, which represent a heterogeneous population of different ages, typically older than  $\sim 1$  Gyr, after the dissolution of their parent clusters.

The pioneering discovery of the Hyades stars as

strong X-ray emitters showing coronal luminosities up to two orders of magnitude higher than that of the solar corona was made with the *Einstein* Observatory. Stern et al. (1981) reported X-ray detections for roughly half of the 85 Hyades stars observed within a 5° field centered on the cluster core. Typical X-ray luminosities of solar-type (G) stars were found to be around  $10^{29}$  erg s $^{-1}$ . Subsequent studies with the same observatory extended the analysis to the outer regions of the cluster (Micela et al., 1988), where X-ray emission was detected from about half of the known Hyades members — 66 out of 121 stars — and detailed X-ray luminosity function of main-sequence stars as a function of color was constructed. However, observations with the *Einstein* Observatory were limited in time coverage and could not encompass the entire cluster. A complete X-ray survey of the Hyades region became possible with the launch of the *ROSAT* mission. Stern et al. (1995) reported X-ray detections within a 900 deg $^2$  field centered on the cluster, as part

\*e-mail: irek\_khamitov@hotmail.com

of the *ROSAT All-Sky Survey* (RASS). More than 185 optically identified Hyades stars were detected, down to limiting X-ray luminosities of  $\approx (1\text{--}2) \times 10^{28}$  erg s $^{-1}$ . The detection completeness for G-type Hyades members in the RASS was approximately 90%. A comparison with *Einstein* data revealed only moderate long-term variability in stellar X-ray luminosities, within a factor of about two. Follow-up pointed *ROSAT* observations with exposure times of  $\sim 20\text{--}40$  ks covered an area of  $\sim 3.5$  deg $^2$  around the cluster (Pye et al., 1994), reaching limiting luminosities as low as  $L_X \sim 5 \times 10^{27}$  erg s $^{-1}$  in the 0.1–2.4 keV energy band. The detection completeness reached approximately 75%. The derived X-ray luminosity function showed that the luminosities of dK binary stars in the Hyades significantly exceed those of single dK stars.

With the advent of new high-precision optical data and refined membership lists for the Hyades cluster, the archival X-ray datasets from *ROSAT* and other observatories accumulated over the past three decades have been repeatedly revisited. Freund et al. (2020) combined data from the *ROSAT*, pointed *ROSAT* observations, and archival observations with *Chandra* and *XMM-Newton* covering both the core and the tidal tails of the Hyades. In total, X-ray emission was detected from 281 sources among 1066 confirmed Hyades members. The detection fraction reached 72% for F- and G-type stars, while for K- and M-type stars it decreased to 22%.

Later, Núñez et al. (2022) used *ROSAT*, *Chandra*, *Swift*/Neil Gehrels, and *XMM-Newton* data to perform a comprehensive cross-match of X-ray sources with an updated Hyades membership list based on *Gaia* DR2 and pre-*Gaia* catalogs. Out of 1315 stars belonging to both the cluster core and its tidal tails, 462 were identified as X-ray sources. By analyzing the relation between the Rossby number ( $Ro$ ) and the fractional X-ray luminosity ( $L_X/L_{\text{bol}}$ ), the authors derived a power-law slope in the range of  $-3.2$  to  $-3.9$  for single stars in the unsaturated regime. They also demonstrated that binarity has only a minor effect on the derived slope.

The Hyades are located at Galactic coordinates  $l = 179^\circ 6565$ ,  $b = -21^\circ 7361$ , nearly on the boundary between the sky regions observed by the Russian and German *e*ROSITA consortia. The eastern Galactic hemisphere contains 405 Hyades members, and the western one 385 members. In this work, we performed a cross-identification between point sources of the X-ray all-sky survey conducted with the *e*ROSITA X-Ray telescope (Predehl et al., 2021) onboard the SRG orbital observatory (Sunyaev et al., 2021), and the updated catalog of Hyades members based on *Gaia* DR3 data (Žerjal et al., 2023). The *e*ROSITA source catalog, combined with archival data from pre-

vious missions, enables long-term studies of stellar coronal activity and flaring behavior in the Hyades over a timescale of up to 30–40 years.

In this study, we focus on the sources located in the eastern Galactic hemisphere, the processing of data on which the Russian consortium of the *e*ROSITA telescope is responsible. Despite this restriction, the properties of the eastern and western subsamples are not expected to differ significantly.

Section 1 describes the cross-identification procedure for the *e*ROSITA X-ray sources in the Hyades. Section 2 presents the catalog of X-ray-bright Hyades members detected by *e*ROSITA. In Section 3, we discuss the properties of X-ray sources located within the tidal radius of the cluster. Section 4 provides a comparison between the *e*ROSITA and *ROSAT* results for the Hyades sources. Finally, Section 5 summarizes our conclusions.

## IDENTIFICATION OF X-RAY SOURCES IN THE HYADES

### *e*ROSITA telescope data

The Hyades region was observed by the SRG/*e*ROSITA observatory partially during four and partially during all five all-sky survey scans. As a result, approximately two thirds of the cluster were observed with a relatively uniform temporal coverage and an exposure time of about  $\sim 550$  s, while the remaining third was observed with an exposure time of  $\sim 750$  s. In the 0.3–2.3 keV energy range, this corresponds to a flux sensitivity of  $F_{X,0.3\text{--}2.3} \sim (6\text{--}8) \times 10^{-15}$  erg s $^{-1}$  cm $^{-2}$ .

To identify X-ray sources associated with the Hyades, we used the *e*ROSITA point-source catalog constructed from the sum of all-sky survey data in the 0.3–2.3 keV band. The X-ray fluxes listed in the *e*ROSITA catalog were recalculated assuming a model of optically thin thermal plasma emission with a temperature of 150 eV and zero neutral hydrogen column density along the line of sight ( $N_{\text{H}} = 0$ ), for the same 0.3–2.3 keV range. For plasma temperatures of 300 eV and 500 eV, the quoted luminosities should be multiplied by correction factors of 0.83 and 0.81, respectively. Moderate column densities of  $N_{\text{H}} \sim 10^{20}$  cm $^{-2}$  change these values by only a few percent. We did not attempt to apply bolometric corrections to the X-ray luminosities due to their large uncertainties. The catalog was filtered using a detection likelihood threshold corresponding to a  $3\sigma$  significance level (likelihood  $\geq 6$ ). In addition, we required that the 98% positional uncertainty radius ( $r98$ ) of the X-ray source satisfies the condition  $r98 < 20''$ . Only sources meeting these criteria were used for further analysis.

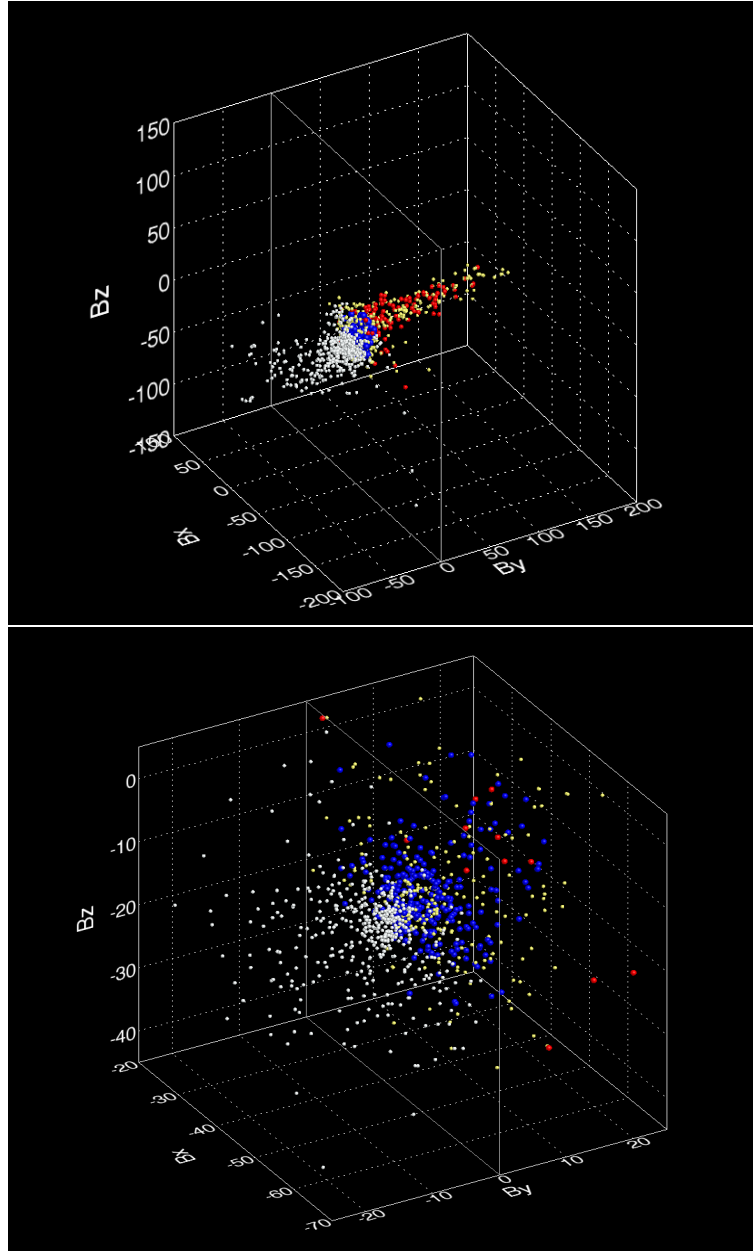


**Fig. 1.** Three-dimensional distribution of stars in the Hyades cluster in Cartesian Galactic coordinates. The  $B_x$  axis points toward the Galactic Center,  $B_z$  is directed toward the north Galactic pole, and  $B_y$  is orthogonal to both  $B_x$  and  $B_z$ ; the  $(B_x, B_y)$  plane coincides with the Galactic disk. The colors indicate the following: light gray — Hyades members located on the western Galactic hemisphere; yellow — Hyades members on the eastern Galactic hemisphere not detected by *eROSITA*; blue and red — Hyades members on the eastern Galactic hemisphere detected by *eROSITA*, located inside and outside three tidal radii ( $R_t = 8.4$  pc), respectively. The schematic plane dividing the sky into the eastern and western Galactic hemispheres is also shown. *Top panel:* the overall view of the Hyades cluster with its extended western and eastern tidal tails. *Bottom panel:* the distribution of stars within three tidal radii of the Hyades cluster.

**Table 1.** *eROSITA* X-ray sources associated with Hyades stars

SRGe+	Gaia DR3+	RA ( $^{\circ}$ )	DEC ( $^{\circ}$ )	G (mag)	$r_{98}$ ( $''$ )	sep ( $''$ )	N	$L_X$	$L_X\text{-}err$	$\log \frac{L_X}{L_{bol}}$ (dex)	$X_{var}$	<i>SpT</i>
J022738.8+174022	85631619134557952	36.9115	17.6723	13.5	4.1	1.9	1	3.48	0.44	-3.31	> 14.4	M3V
J023430.1+361310	327351657000000128	38.6242	36.2194	16.2	7.2	2.7	1	0.61	0.12	-3.02	> 8.6	M5.5V
J024612.3+055628	6531412602259712	41.5528	5.94059	15.3	8.9	5.9	1	0.49	0.15	-3.56	> 1.7	M4.5V
J024820.8+235217	113045124074462976	42.0862	23.8718	14.0	5.9	1.8	1	1.45	0.21	-3.38	2.0	M4V
J025259.2+314646	136304467927526144	43.2461	31.7791	15.3	4.8	1.3	1	1.67	0.25	-3.03	2.1	M4.5V
J025641.5+352230	140340019198719232	44.1730	35.3759	12.5	6.4	3.7	1	0.89	0.16	-4.01	> 2.8	M2.5V
J025746.8+293941	129070265532645888	44.4454	29.6612	8.7	3.4	1.7	1	4.13	0.34	-4.60	1.8	K1V
J025805.4+204008	108421608959951488	44.5228	20.6685	5.7	2.8	1.7	1	5.29	0.31	-5.47	1.3	F5V

The full table is available in the archive of the Strasbourg Astronomical Data Center (CDS).

Columns are defined as follows: (1) source designation in the *SRG/eROSITA* catalog; (2–5) Gaia DR3 identifier, right ascension and declination in degrees (J2000.0), and *G*-band magnitude; (6)  $r_{98}$  — the 98% positional uncertainty radius of the *eROSITA* source (arcsec); (7) angular separation between the X-ray and optical positions (arcsec); (8)  $N$  — the total number of Gaia DR3 optical sources within  $r_{98}$ ; (9) X-ray luminosity estimate from the five *eROSITA* surveys in the 0.3–2.3 keV band, in units of  $\times 10^{28}$  erg s $^{-1}$ ; (10) uncertainty of the X-ray luminosity, in units of  $\times 10^{28}$  erg s $^{-1}$ ; (11) logarithm of the ratio  $L_X/L_{bol}$  from the five *eROSITA* surveys in the 0.3–2.3 keV band; (12)  $X_{var}$  — X-ray variability factor, defined as the ratio of maximum to minimum flux measured across the five *eROSITA* surveys, accounting for flux measurement uncertainties; (13) *SpT* — spectral type of the star.

### Identification of optical components

For the identification of *eROSITA* X-ray sources in the Hyades, we used the most complete and extensive catalog of members of nearby open clusters to date, including the Hyades, as presented by Žerjal et al. (2023). The selection of cluster members in this catalog is based on the exceptional astrometry of *Gaia* DR3, either in five-dimensional or full six-dimensional space (spatial and kinematic parameters). Hereafter, we refer to this as the “6d catalog”. The difference between the five- and six-dimensional selections is due to the presence or absence of radial velocity measurements. Within the tidal radius of the cluster ( $r_{\text{tidal}} = 8.4 \pm 0.02$  pc), 427 so-called bona fide members were identified. Overall, the 6d catalog of the Hyades contains members out to three tidal radii from the cluster center, for a total of 790 stars. However, all stars brighter than  $G < 5^m$  were excluded from the 6d catalog due to instrumental limitations of the *eROSITA* detectors related to ultraviolet light leaks. Furthermore, since the Russian *eROSITA* consortium is responsible for the processing of observations in the eastern Galactic hemisphere, only Hyades members in this sky region were considered. As a result, 395 stars from the 6d catalog were used for further analysis. We note that this restriction approximately divides the Hyades sample equally between the eastern and western Galactic hemispheres (395 vs. 370 sources). Within the tidal radius, this division corresponds to 214 and 196 stars, respectively, making the two subsamples statistically comparable. Our study focuses

on the analysis of Hyades members located within the tidal radius in the eastern Galactic hemisphere.

Detailed studies based on *Gaia* DR2 data led to the discovery of tidal tails associated with the Hyades cluster (Meingast & Alves, 2019; Röser et al., 2019) within 200 pc from the Sun. The improved astrometric precision in the third *Gaia* release (DR3) allowed the sample of stars associated with the Hyades tidal tails to be extended out to 400 pc (Jerabkova et al., 2021). Candidates for the Hyades tidal tails within 200 pc were published in the catalogs *J/A+A/621/L2* (Röser et al., 2019) containing 1316 sources, and *J/A+A/621/L3* (Meingast & Alves, 2019) containing 238 sources. To identify matches between sources in the eastern Galactic tidal tail and *eROSITA* X-ray sources, we constructed a sample from these catalogs including all sources located beyond three tidal radii of the cluster with Galactic longitude  $0^{\circ} < l < 180^{\circ}$ . This sample comprises 281 sources and is hereafter referred to as *ett200* (Eastern Tidal Tail within 200 pc). The study of tidal tail candidates at distances greater than 200 pc will be addressed in future work.

The *eROSITA* X-ray source catalog was cross-matched with both the 6d and *ett200* catalogs of Hyades members, using the 98% positional uncertainty radius of the X-ray source ( $r_{98}$ ) as the matching criterion. A total of 290 *eROSITA* sources were found to contain at least one Hyades star within their error circles; for 15 *eROSITA* sources, two Hyades members were located within the error circle. The mean expected number of chance coincidences when correlating the *eROSITA* catalog with the Hyades catalog

is 0.92. To estimate the number of random matches, the positions of the optical sources were shifted by 6' in a random direction, and the resulting catalog was correlated with the *eROSITA* catalog. This procedure was repeated 200 times and the results were averaged. In the Hyades tidal tail, 114 *eROSITA* sources were identified, with only one source containing two tidal tail members within its  $r_{98}$  error circle.

Figure 1 shows the three-dimensional distribution of stars in the Hyades cluster in Cartesian Galactic coordinates. The  $Bx$  axis points toward the Galactic Center,  $Bz$  is directed toward the north Galactic pole, and  $By$  is orthogonal to both  $Bx$  and  $Bz$ , with the  $(Bx, By)$  plane coinciding with the Galactic disk. The colors indicate the following: light gray — Hyades members located on the western Galactic hemisphere; yellow — Hyades members on the eastern Galactic hemisphere not detected by *eROSITA*; blue and red — Hyades members on the eastern Galactic hemisphere detected by *eROSITA*, located inside and outside three tidal radii ( $R_t = 8.4$  pc), respectively. The schematic plane dividing the sky into eastern and western Galactic hemispheres is also shown. *Top panel*: overall view of the Hyades cluster with extended western and eastern tidal tails. *Bottom panel*: distribution of stars within three tidal radii of the Hyades cluster.

#### CATALOG OF X-RAY BRIGHT STARS IN THE HYADES BASED ON *EROSITA* DATA WITHIN 3 TIDAL RADII

A part of the catalog, comprising 290 *eROSITA* X-ray sources associated with Hyades stars located within three tidal radii, is presented in Table 1. The full catalog will be made available in electronic form at the Strasbourg Astronomical Data Center (CDS).

The absolute magnitude ( $MG$ ) in the *Gaia* DR3  $G$  band and the X-ray luminosity were calculated using the *Gaia* DR3 parallax for each source. The bolometric luminosity and spectral types were estimated by interpolating the dependence of these parameters on  $MG$  for main-sequence stars. For this purpose, we used the Mamajek tables (Version 2022.04.16), originally published in Pecaut & Mamajek (2013). In the same way, estimates of the effective temperature ( $T_{\text{eff}}$ ) and stellar mass in units of solar masses ( $M/M_{\odot}$ ) were obtained.

Information on binarity for the Hyades stars was compiled from several sources. We used the catalog of (Núñez et al., 2022), which provides a binarity parameter  $bin$ : 1 — candidate binaries, and 2 — confirmed systems. In our subsequent analysis we treated both confirmed binaries and candidates as binary systems. We also used the results of Žerjal et al. (2023), from which we extracted all objects flagged with the *binary1* or *binary2* parameters, as well as the cata-

log of stellar and substellar companions in the Hyades by (Gratton et al., 2025). According to these catalogs, the total number of sources with evidence for binarity is 140. To this list, we added 47 sources with excess astrometric noise ( $RUWE > 1.4$ ) in the *Gaia* DR3 data that were not included in the above catalogs; we assumed these to be additional likely binaries. In addition, two sources marked as binary or multiple systems in the SIMBAD database were added: *Gaia DR3* 37414254686537344 and *Gaia DR3* 221991882981235072. It should be noted that at the distance of the Hyades, the most compact binaries with periods of about 10 days or less exhibit astrometric perturbations that are too small, resulting in low  $RUWE$  values (Torres et al., 2024). Therefore, a small contamination of the single-star sample still remains. With this rather optimistic approach, 189 out of 395 optical sources are classified as binary, i.e. slightly less than half. In the electronic version of Table 1, the binarity parameter *bflag* is included, where 0 denotes single stars and 1 denotes systems with binarity.

When determining  $L_{\text{bol}}$ ,  $SpT$ ,  $T_{\text{eff}}$ , and  $M/M_{\odot}$ , we did not account for the binarity of the sources. In particular, the assumption that stars are single may lead to inaccurate *Gaia* solutions for unresolved binaries and complicate their classification as cluster members. In general, note that for systems with mass ratios  $q$  close to 1, the parameter  $R_X = L_X/L_{\text{bol}}$  will not be significantly affected (the X-ray luminosity increases approximately in the same way as the bolometric luminosity for such systems). In contrast, systems with low mass ratios  $q$ , given comparable absolute X-ray luminosities of the early- and late-type components (Fig. 8), may lead to an underestimation of  $R_X$  — approximately in proportion to the ratio of the bolometric luminosities of the components of the binary system. On the color-magnitude diagram, in the limiting case of spectroscopic binaries with  $q \sim 1$ , the observed absolute magnitude ( $MG$ ) will be shifted by about 0.75 mag. A small group of such photometric binaries can be clearly seen slightly above the main sequence in Fig. 2.

In the electronic version of Table 1, the column  $N_{6d}$  lists the number of Hyades members located within  $r_{98}$  of the *eROSITA* source position. For sources with  $N_{6d} > 1$ , the angular resolution of the *eROSITA* telescopes is insufficient for an unambiguous identification of the optical counterpart.

The X-ray variability factor  $X_{\text{var}}$  was determined in the same way as in our study of the Pleiades cluster (Khamitov et al., 2024), namely as the ratio between the maximum and minimum fluxes measured across the 4–5 all-sky scans. The fluxes in individual scans were derived using forced PSF photometry. In this procedure, the distribution of counts in

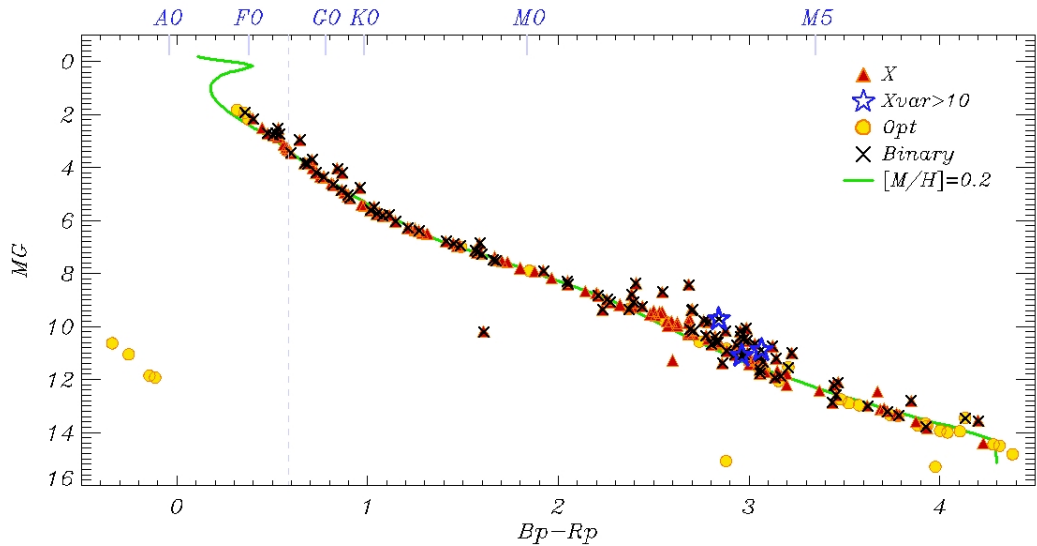


**Fig. 2.** Color–absolute magnitude diagram ( $Bp-Rp$  vs.  $M_G$ ) for Hyades sources within the tidal radius. Red triangles indicate stars detected in X-rays by *eROSITA*, while yellow circles mark stars with X-ray luminosities below the *eROSITA* sensitivity. Black crosses denote sources with confirmed binarity (see text). The green line shows the isochrone computed using the *PARSEC v1.2S* models (Bressan et al., 2012) for a fixed stellar age of 700 Myr. The vertical dashed line marks the approximate boundary of main-sequence stars possessing a convective zone. Blue stars indicate X-ray sources exhibiting strong variability ( $X_{var} > 10$ ).

the X-ray image was approximated by the telescope’s point-spread function, taking into account the background map. The approximation was performed via maximum-likelihood fitting assuming Poisson count statistics, while the source position was fixed to the coordinates obtained from the coadded data of all scans; thus, the only free parameter of the fit was the source flux. When selecting the maximum and minimum flux values, we used the measured flux in those scans where the detection likelihood was at least 6 (corresponding to a significance level of approximately  $3\sigma$  for a Gaussian distribution). If in a given scan the source did not reach a likelihood of 6, then a  $3\sigma$  upper limit to the flux was used for determining the minimum flux, while this scan was not used when determining the maximum flux. If the source did not exceed a likelihood of 6 in any of the all-sky scans, the value of  $X_{var}$  was considered undefined.

#### PROPERTIES OF STARS WITH X-RAY EMISSION WITHIN THE TIDAL RADIUS OF THE HYADES CLUSTER.

To investigate the properties of X-ray-emitting stars in the Hyades, we restricted our analysis to the region within the tidal radius (8.4 pc). A total of 213 stars from the 6D catalogue fall within this selection. The number of *eROSITA* sources associated with Hyades stars is 168, with 9 of these sources having two Hyades members within  $r98$ . Thus, the full number of X-

ray-active stars lies in the range 168–177, and consequently the *eROSITA* detection fraction for Hyades stars inside the tidal radius is approximately  $79\%–83\% \pm 3\%$  (the uncertainty was estimated under the assumption of a binomial distribution of the number of X-ray sources). Compared to the fraction of *detected* X-ray-active stars in the Pleiades ( $\sim 50\%$ , Khamitov et al. 2024), this detection rate is high, despite the fact that the Pleiades are significantly younger than the Hyades and exhibit greater coronal activity. This difference is explained by the proximity of the Hyades: the achieved limiting luminosity sensitivity is an order of magnitude deeper than that reached in the Pleiades.

#### Color-luminosity diagram

The colour–luminosity diagram for stars within the tidal radius of the Hyades is shown in Fig. 2. In this diagram, stars with detected X-ray emission are marked by red triangles, while stars not detected by *eROSITA* are shown as yellow circles. Sources identified as binaries are marked with black crosses. In addition, stars with an X-ray variability factor  $X_{var} > 10$  — i.e. sources showing X-ray flux variations exceeding an order of magnitude—are indicated by blue symbols. Notably, all strongly variable X-ray sources belong to M-dwarf stars.

The metallicity of Hyades stars has been extensively studied using spectroscopic and photometric methods, as well as through isochrone fitting. A comprehensive analysis of existing measurements is presented,

**Table 2.** Upper limits of X-ray luminosity for single WDs within the Hyades tidal radius.

GAIA DR3+	RA ( $^{\circ}$ )	DEC ( $^{\circ}$ )	$L_X$ $\times 10^{27} \text{ erg/s}$
39305036729495936	60.9260	14.9912	1.4
45980377978968064	62.3709	17.1317	2.0
3313606340183243136	65.9826	16.3541	2.1
3313714023603261568	67.1647	16.9699	2.5

for example, in Netopil et al. (2016) and Brandner et al. (2023), and the references therein. These results show a metallicity range of approximately  $[M/H] = 0.15\text{--}0.25$  dex.

In Fig. 2, the green curve shows an isochrone computed using the *PARSEC v1.2S* models (Bressan et al., 2012) for a fixed stellar age of 700 Myr and a metallicity of  $[M/H] = 0.2$ . This isochrone provides a good representation of the Main Sequence (MS) of the Hyades cluster.

In Fig. 2, a group of sources located above the observed MS is also clearly visible; these are the so-called photometric binary systems.

Due to the selection criteria used, the seven optically brightest Hyades stars ( $G < 5^m$ ) were not included in the sample. These are  $\delta^1 \text{Tau}$ ,  $\delta^2 \text{Tau}$ ,  $\delta^3 \text{Tau}$ ,  $\gamma \text{Tau}$ ,  $\epsilon \text{Tau}$ ,  $\kappa \text{Tau}$ , and  $\nu \text{Tau}$ , and thus they are not represented in the color-luminosity diagram.

We did not detect X-ray emission from four single white dwarfs (WDs) located within the tidal radius of the Hyades. Table 2 presents the upper limits on the X-ray luminosity of these WDs in the 0.3–2.3 keV energy range, which were derived based on the eROSITA sensitivity at the positions of these objects and the high-precision parallax measurements from the Gaia observatory.

#### Distribution of X-ray emitting stars in the Hyades by spectral types

X-ray-emitting stars are detected across a wide spectral range, from early F-type to late M dwarfs (M7V). Notably, all F, G, and early K-type stars were detected by *eROSITA*. In Fig. 2, this boundary is indicated by a vertical dashed line. The absence of X-ray sources at the faint end of the main sequence, among stars with absolute magnitude fainter than 14, is due to the sensitivity limit of *eROSITA*.

The distribution of stars within the tidal radius of the Hyades in the eastern Galactic hemisphere by spectral type is shown in Fig. 3. The figure shows distributions for all stars and for X-ray-detected stars. Histograms are binned by absolute magnitude with a bin size of  $1.5^m$ . As in Fig. 2, the vertical dashed line

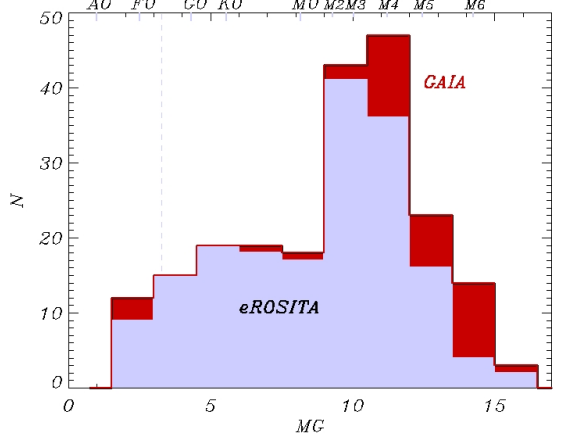


**Fig. 3.** Distribution of stars by absolute magnitude (MG). Sample of Hyades stars in the eastern Galactic hemisphere within the cluster's tidal radius (8.4 pc). The red histogram shows the distribution for the full 6d-catalog sample (GAIA), while the gray histogram represents X-ray-detected stars according to *eROSITA* data. The vertical dashed line indicates the approximate boundary of stars with a convective zone.

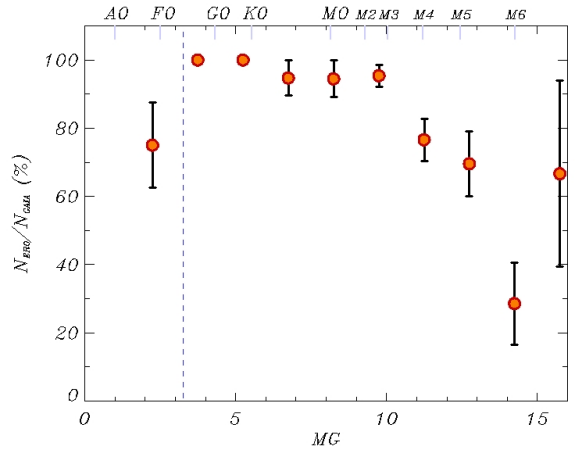


**Fig. 4.** Fraction of X-ray-emitting stars in the eastern Galactic hemisphere within the tidal radius of the Hyades as a function of absolute magnitude (MG). The vertical dashed line indicates the approximate boundary of stars with a convective zone.

**Table 3.** Fraction of X-ray-emitting Hyades stars across spectral ranges in the eastern Galactic hemisphere within the tidal radius of 8.4 pc. The columns correspond to the selected spectral range and have the following meaning: MG — the interval of absolute magnitudes in the Gaia DR3  $G$  band;  $N_{\text{opt}}$  — total number of optical sources;  $N_X$  — number of sources detected in X-rays by *eROSITA*;  $N_X/N_{\text{opt}}$  — percentage of stars with detected X-ray emission;  $\sigma$  — standard deviation of the X-ray detection fraction.  $L_X$  is the median X-ray luminosity in the 0.3–2.3 keV band for the given spectral class, in erg s $^{-1}$ .

Spectral range	MG	$N_{\text{opt}}$	$N_X$	$N_X/N_{\text{opt}}$ (%)	$\sigma$ (%)	$L_X$ ( $\times 10^{28}$ )
earlier F0	< 2.51	4	1	25.0	21.7	4.8
F0-F5	2.51–3.26	10	10	100.0	0.0	8.7
F5-G0	3.26–4.325	10	10	100.0	0.0	12.1
G0-K0	4.325–5.553	15	15	100.0	0.0	7.1
K0-K5	5.553–6.83	16	16	100.0	0.0	2.3
K5-M0	6.83–8.16	17	15	88.2	7.8	0.8
M0-M1	8.16–8.82	9	9	100.0	0.0	9.7
M1-M2	8.825–9.29	7	7	100.0	0.0	0.9
M2-M3	9.29–10.05	22	20	90.9	6.1	5.7
M3-M4	10.05–11.21	39	34	87.2	5.4	2.1
M4-M5	11.21–12.45	29	22	75.9	7.9	0.8
later M5	> 12.45	35	18	51.4	8.4	0.6
total		213	177	83.1	2.6	

indicates the approximate boundary of main-sequence stars with a convective zone.

Figure 4 shows the fraction of stars with X-ray emission as a function of spectral type. Errors in each bin were calculated assuming a binomial distribution of the number of X-ray sources<sup>1</sup>. The results of counting the fraction of X-ray-emitting stars in broad spectral range intervals are given in Table 3.

Considering the detectability of X-ray emission, Table 3 and Figs. 3 and 4 allow us to distinguish three spectral intervals: (1) stars earlier than F0, (2) stars from F0 to M4, and (3) stars later than M4. The first group is characterized by the absence of a convective envelope and intrinsically low X-ray luminosity, despite their high optical brightness. Consequently, the number of stars detected by *eROSITA* in this group is limited by the survey sensitivity. These include four A-type stars (GAIA DR3 IDs: 145391484855481344, 145484634106814592, 3311883817778820480, and 3313842529024545664). X-ray emission is detected for only one source, GAIA DR3 33313842529024545664 (also known as 63 Tau, HD 27749; SRGe J042325.2+164640), with an estimated X-ray luminosity of  $L_X = 4.8(5) \times 10^{28}$  erg s $^{-1}$ . This star is also a spectroscopic binary. The limit-

ing sensitivity achieved by *eROSITA* for the remaining three stars of this group is  $\sim 3.5 \times 10^{27}$  erg s $^{-1}$ . Given that the typical X-ray luminosity of A-type stars (Drake et al., 2014; Günther et al., 2022) is much lower than that of SRGe J042325.2+164640, the observed X-ray emission is likely produced by the secondary component of the binary system. Indeed, Gratton et al. (2025) derived component masses and the semi-major axis:  $M_A = 1.72 M_\odot$ ,  $M_B = 0.85 \pm 0.4 M_\odot$ ,  $a = 0.097 \pm 0.097$  au, indicating that the X-ray source may be a G- or K-type star. However, the system may also be intrinsically active due to the small orbital separation. This system is listed among Hyades candidates with significant astrometric and spectroscopic excess noise in *Gaia* data. An analysis of this list was also carried out in the context of the search for stellar-mass black holes in the Hyades (Torniamenti et al., 2023). In total, 18 such high-noise sources are identified in our Hyades sample, almost all within the tidal radius (only one lies at the  $1\sigma$  boundary). Stars of M spectral type in this first group exhibit high levels of X-ray emission relative to their bolometric luminosity,  $L_X/L_{\text{bol}} \sim 10^{-3}$ , whereas earlier-type stars show values 1.5–2 orders of magnitude lower.

The second interval spans a wide range of spectral types and exhibits a high fraction of stars with X-ray emission, exceeding  $\sim 90$ –100%. It should be noted that sources in this group with spectral types earlier than F5 lack a convective zone, and the X-ray emission from these sources requires separate investigation. In the third spectral type interval, the absolute luminosities of stars in both the optical and X-ray bands decrease, and the number of stars detected by *eROSITA* is limited by the survey’s sensitivity. Of course, the lack of X-ray emission from individual sources while stars of the same type (mass) are confidently detected may be due to an incorrect classification of their membership in the Hyades. Field stars are on average older, less active, and have lower X-ray luminosity.

#### X-ray luminosity function

Figure 5 shows the distribution of X-ray luminosities for *eROSITA* sources in the Hyades within the cluster’s tidal radius. The distributions were binned in 0.3 dex intervals for all sources (gray line), as well as separately for binary systems (green line) and single stars (yellow line). These distributions confirm earlier findings from *ROSAT* for dK stars (Pye et al., 1994), namely that binaries tend to exhibit higher X-ray luminosities on average than single dK stars. The new *eROSITA* data extend this result to later dM spectral types in the Hyades. It is well known that the fraction of binary stars in a sample increases with mass (see, e.g., Offner et al. (2023)), and therefore single stars are on average less massive than the primary compo-

<sup>1</sup>If  $N_{\text{gaia}}$  is the total number of sources in a bin, of which  $N_{\text{ero}}$  are detected in X-rays, then  $p = N_{\text{ero}}/N_{\text{gaia}}$  is the estimated fraction of X-ray-emitting stars in that bin. Assuming a binomial distribution, the expected variance is  $\text{Var}(N_{\text{ero}}) = N_{\text{gaia}} \cdot p \cdot (1 - p) = N_{\text{ero}} \cdot (1 - N_{\text{ero}}/N_{\text{gaia}})$ . Therefore,  $\sigma = \sqrt{N_{\text{ero}} \cdot (1 - N_{\text{ero}}/N_{\text{gaia}})}$ .

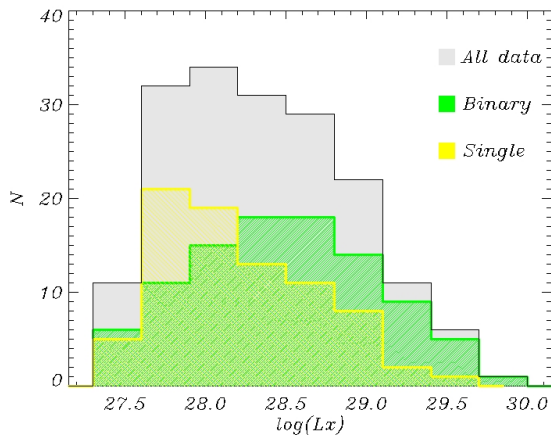


**Fig. 5.** Distribution of stars in the Hyades by the logarithm of X-ray luminosity, as detected by eROSITA. The full sample of sources is shown in gray, binaries are shown in green, and single stars are shown in yellow.

nents of binary or multiple systems. In the studied sample, low-mass M-dwarfs dominate, which is a natural consequence of the initial mass function. However, among M-type stars with detected X-ray emission, the fraction of binaries is comparable to that of single stars of this type. This difference in luminosity distributions most likely reflects the fact that in binary systems observed in the saturated regime, angular momentum loss occurs through orbital motion, allowing the sources to remain bright in the X-ray range. In the unsaturated regime, a mass selection effect is present in binary systems, where higher-mass stars appear more luminous.

#### X-ray variability

Figure 6 shows the dependence of the X-ray variability parameter  $X_{var}$ , introduced above, on absolute magnitude (left panels) and peak X-ray luminosity (right panels). Sources for which only a lower limit on  $X_{var}$  could be determined are indicated by red arrows. The top panels display all stars detected by eROSITA within the tidal radius in the eastern Galactic hemisphere. The middle and bottom panels show the same sources, but separated into single stars and binaries, respectively. These plots demonstrate that the amplitude of variability is higher for M-dwarf stars. A detailed study of X-ray variability and flare activity among Hyades stars will be presented in a separate paper.

For six Hyades stars, X-ray variability with  $X_{var} \geq 10$  has been registered. Three of these are located within the cluster's tidal radius: SRGe J035453.3+161856, SRGe J041305.7+151452, and SRGe J042135.8+165339. Figure 7 shows the X-ray

light curves of these sources, constructed from individual all-sky scans. The blue line indicates the X-ray flux level estimated from the sum of all catalogs. Notably, all strongly variable sources are late-type M-dwarf stars that are binaries. Their pronounced X-ray variability is primarily associated with stellar flares, which will be the subject of a separate study.

As can also be seen from Fig. 6 (right panel), for sources with peak X-ray luminosities below  $\sim 10^{28}$  erg s $^{-1}$ , only lower limits on the variability factor  $X_{var}$  are available. This is because the detection threshold in a single scan is roughly three times higher than the sensitivity achieved from the full dataset, and can exceed  $\sim 5 \times 10^{27}$  erg s $^{-1}$ . Due to intrinsic variability and/or Poisson fluctuations, sources fainter than  $\sim 10^{28}$  erg s $^{-1}$  may go undetected in at least one scan, and according to the definition of  $X_{var}$ , only a lower limit on this parameter can be obtained for such sources.

#### Dependence of the X-ray luminosity of Hyades stars on the effective temperature

As noted above, eROSITA data reveal a high fraction of stars detected in X-rays. This is clearly illustrated by the dependence of X-ray luminosity on effective temperature for Hyades stars, shown in Fig. 8. For non-detected sources, gray symbols indicate upper limits on the X-ray luminosity. Across a broad range of spectral types from F0 to K5, all Hyades stars exhibit X-ray emission above  $\sim 2 \times 10^{28}$  erg s $^{-1}$ . While the distribution of early-type stars without a convective zone (the approximate boundary of convective stars is shown by the vertical dashed line) appears rather scattered, FGK stars separate into two branches of similar activity levels in terms of  $R_X = \log(L_X/L_{bol})$ . These activity levels are indicated by red lines in Fig. 8. A similar dependence is also observed for the Pleiades (Khamitov et al. 2024). Moreover, while in the Hyades both the left and right branches have a maximum around  $2 \times 10^{29}$  erg s $^{-1}$ , such that M0 stars and late-F stars exhibit the same X-ray luminosity, in the Pleiades the right branch extends to higher values, producing a maximum of X-ray emission for Sun-like stars.

In Fig. 8, for the three strongly variable sources with  $X_{var} > 10$  (see Fig. 7), we illustrate how their position on the diagram changes if the survey containing a flare is excluded. Their quiescent luminosities are shown as light blue open diamonds, and a solid blue line connects these points to the measurements obtained from all surveys, including the flare.

With the exception of two sources — one located within the tidal radius (SRGe J042829.0+174145) and the other (SRGe J041156.5+233809) slightly outside at a distance of  $\sim 9.7$  pc from the cluster cen-

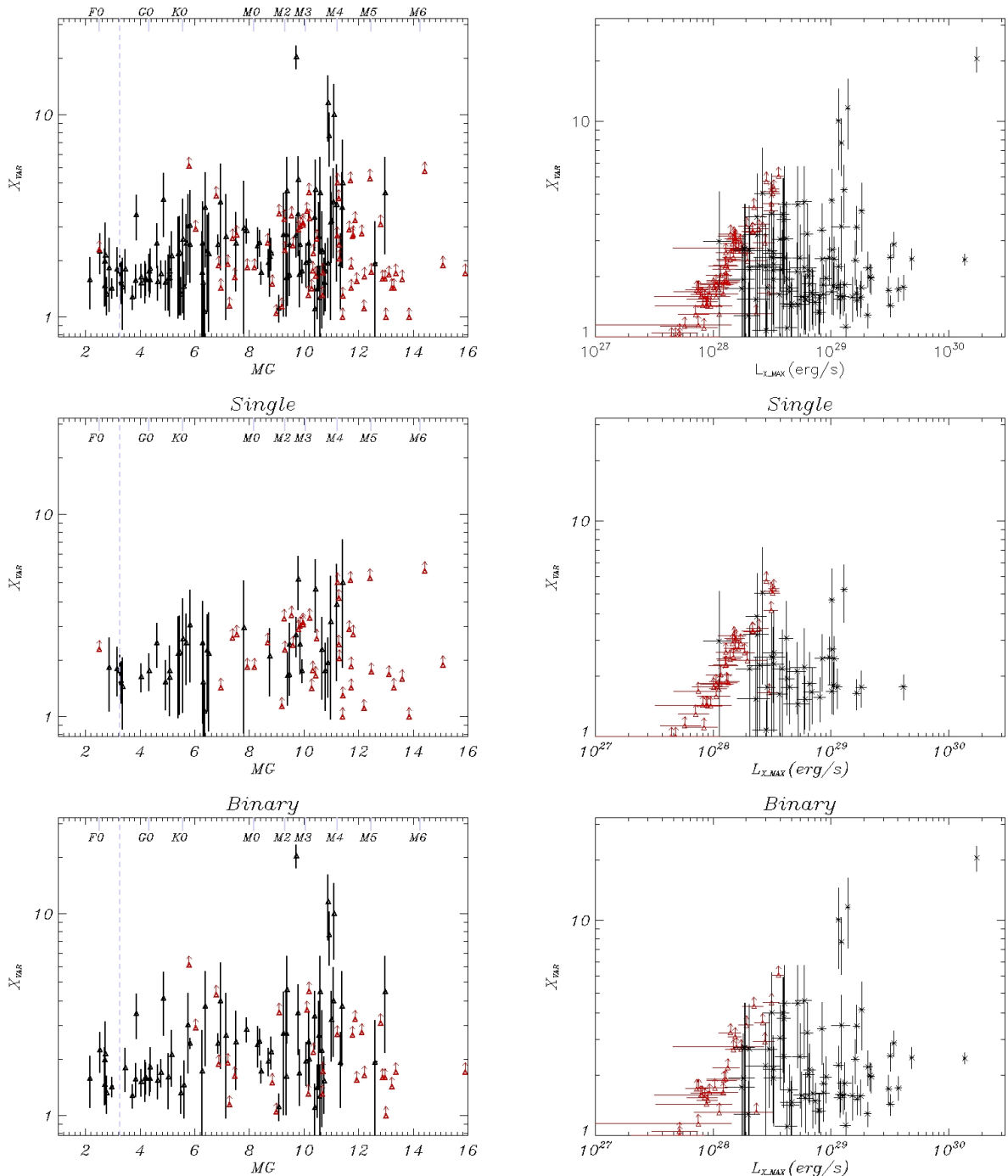


**Fig. 6.** Dependence of the X-ray variability parameter  $X_{var}$  on absolute magnitude (left panel) and peak X-ray luminosity (right panel). Red arrows indicate lower limits on  $X_{var}$  for sources not detected in their minimum-flux state. In the left panel, the dashed vertical line marks the approximate boundary separating stars with convective zones.

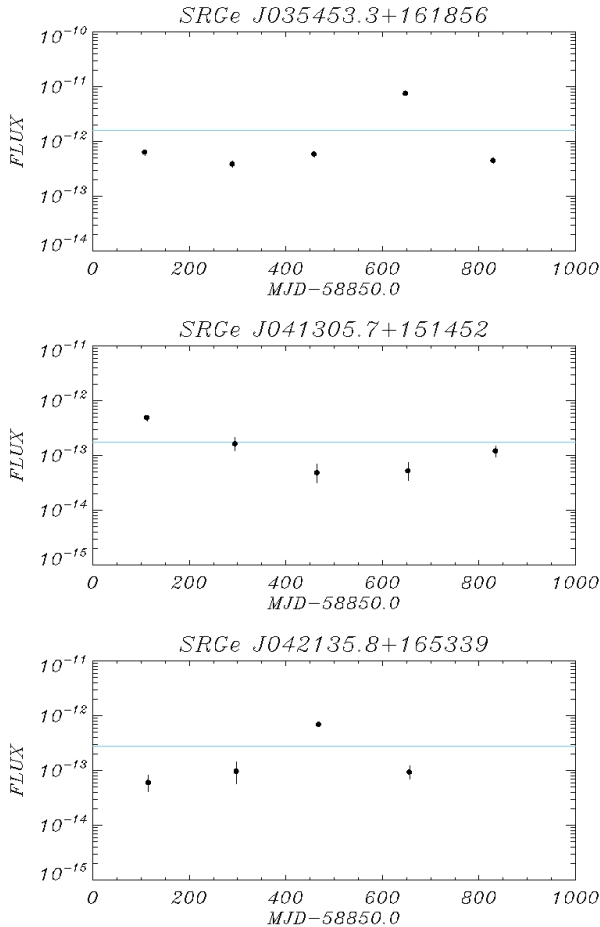


**Fig. 7.** Light curves of highly X-ray variable sources ( $X_{var} > 10$ ). Fluxes are given in units of  $\text{erg s}^{-1} \text{cm}^{-2}$  in the 0.3–2.3 keV energy band. The blue line indicates the X-ray flux estimated from the sum of all surveys.

ter — the X-ray luminosity of single M-type Hyades stars does not exceed  $L_X < 10^{29} \text{ erg s}^{-1}$ . For the X-ray source SRGe J041156.5+233809, two Hyades stars fall within  $r98$ : one M-type star (Gaia DR3 149767987808179968) and one K-type star (Gaia DR3 149767987810042624). The K-type star is known as an RS CVn-type variable (Samus' et al., 2017). For the X-ray source SRGe J042829.0+174145, two Gaia sources are also present within  $r98$ . One belongs to the Hyades (Gaia DR3 3314185129974409088), while the other (Gaia DR3 3314185129975960448) is a field star. According to the GCVS 5.1 catalog of variable stars (Samus' et al., 2017), this field star is an eruptive BY Dra-type variable. Moreover, it has a very high Gaia DR3  $RUWE = 15.09$ , indicating potential binarity, whereas the Hyades star has  $RUWE = 1.15$ . Thus, in both considered *eROSITA* sources, the high X-ray luminosity is attributable to the RS CVn and BY Dra stars rather than single Hyades M-type stars.

The maximum X-ray luminosity among stars within the tidal radius is recorded for the source SRGe J035025.1+171447, with  $L_X \sim 9 \times 10^{29} \text{ erg s}^{-1}$ . This X-ray source is associated with the well-studied precataclysmic binary V471 Tau, consisting of a K2V star and a hot DA white dwarf. The primary star has not yet filled its Roche lobe. The surface coverage of the K star by large magnetic spots is estimated to be about 8–9% (Hussain et al., 2006). Detailed parameters of this system and studies related to V471 Tau can be found, for example, in Muirhead et al. (2022) and references therein. V471 Tau was detected in all five *eROSITA* scans, and its X-ray variability amounted to  $X_{var} \sim 2.3(1)$ .

The X-ray spectrum of V471 Tau is shown in Fig. 9. The spectrum is adequately described (C-statistic 215 for 229 degrees of freedom) by an optically thin, single-temperature plasma model with a temperature of  $kT = 0.81 \pm 0.03 \text{ keV}$  and sub-solar abundances. In particular, the single-temperature model requires sub-solar abundances of oxygen ( $0.32 \pm 0.10$ ), neon ( $< 0.32$ ), magnesium ( $0.27 \pm 0.1$ ), silicon ( $0.27 \pm 0.1$ ), and iron ( $0.096 \pm 0.01$ ). The abundances of the remaining elements are consistent with solar values within the statistical uncertainties. Introducing a second component (i.e., a two-temperature plasma model) does not qualitatively change the elemental abundance pattern and does not significantly improve the fit quality. The temperatures of the components are  $kT = 0.71 \pm 0.03 \text{ keV}$  and  $kT = 1.89_{-0.25}^{+0.43} \text{ keV}$ , with a C-statistic of 206.3 for 228 degrees of freedom. Elemental abundances in this model are oxygen ( $0.36 \pm 0.12$ ), magnesium ( $< 0.30$ ), silicon ( $0.22 \pm 0.15$ ), and iron ( $0.15 \pm 0.03$ ). Abundances of other elements remain consistent with solar values within the statistical uncertainties. The derived coronal abundances of heavy

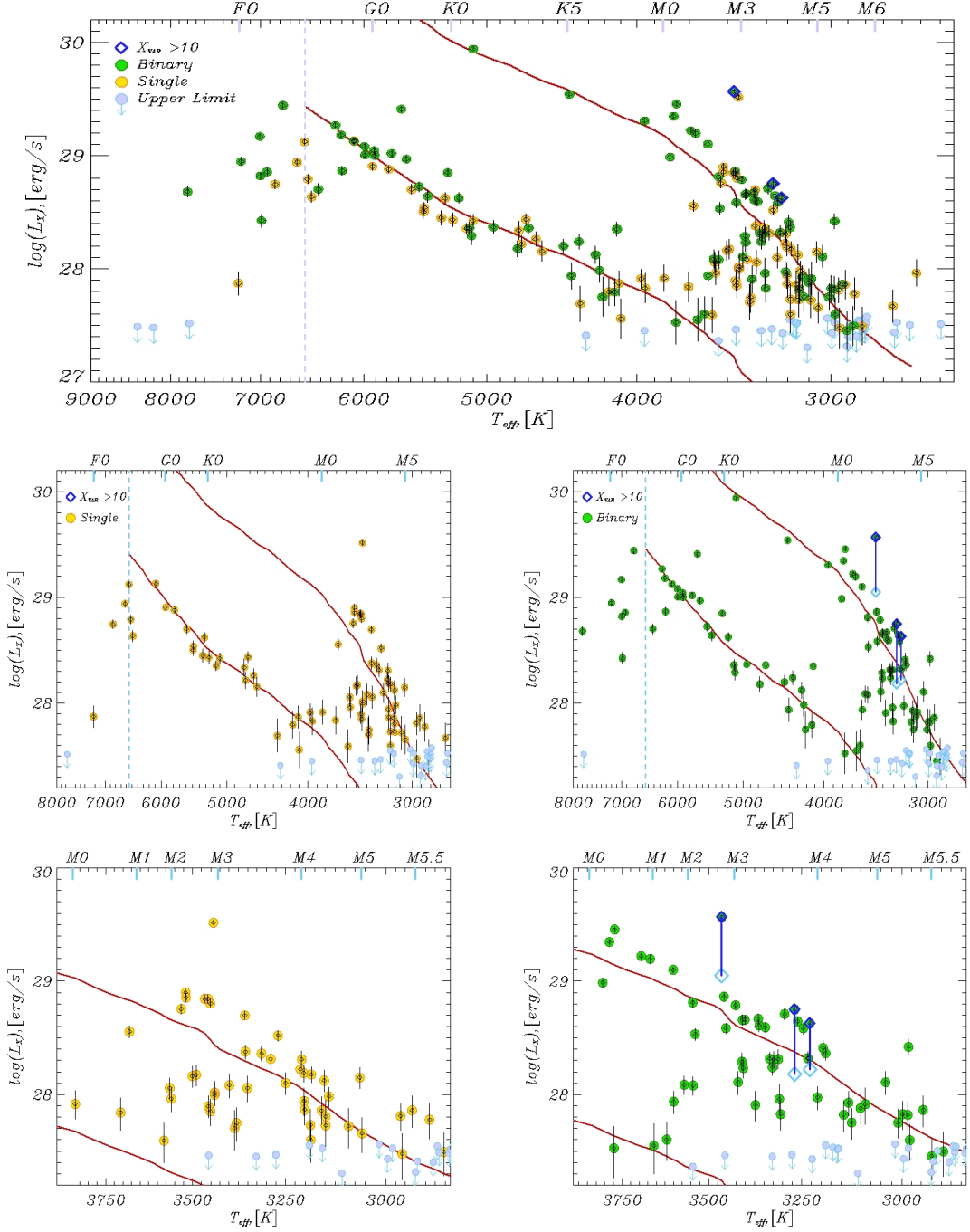


**Fig. 8.** X-ray luminosity of Hyades stars in the 0.3–2.3 keV band, estimated from the sum of all scans, as a function of effective temperature  $T_{\text{eff}}$ . Strongly variable X-ray sources are marked by blue diamonds. Single stars are shown with yellow symbols, binaries with green symbols, and gray symbols indicate upper limits for sources not detected by eROSITA. Red lines correspond to constant  $R_X$  levels matching the peaks in the distribution of this parameter (see Fig. 10). Upper panel: overall view. Middle panels: dependencies for single stars and binaries. Lower panels: same as middle panels, but highlighting the region of late-type stars.

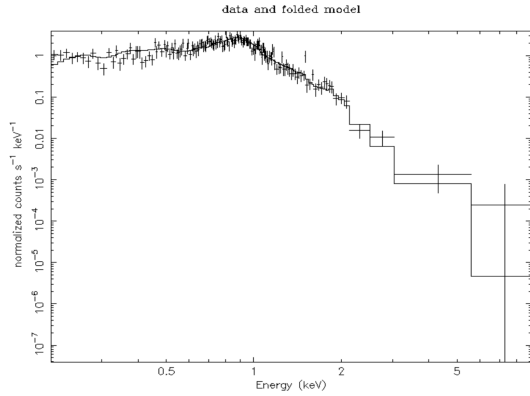


**Fig. 9.** X-ray spectrum of V471 Tau derived from *e*ROSITA data. The spectrum is well described by an optically thin, single-temperature plasma model with a temperature of  $kT = 0.81 \pm 0.03$  keV and sub-solar metal abundances (see text).

elements in V471 Tau differ significantly from optical measurements in the chromosphere and photosphere:  $[Fe/H] = -0.22 \pm 0.02$  dex (Shimansky et al., 2011). A detailed study of X-ray spectra of stars in the Hyades cluster will be presented in a separate paper.

We note that within the full sample, SRGe J035025.1+171447 ranks only second in terms of X-ray luminosity. The highest luminosity is observed for the X-ray source SRGe J041810.9+231704, which is associated with the spectroscopic binary RS CVn system V1313 Tau. This system lies outside the tidal radius at a distance of  $\sim 9.7$  pc from the cluster center, is weakly variable in the X-ray band according to *e*ROSITA ( $X_{var} \sim 1.8$ ), and exhibits an X-ray luminosity of  $L_X \sim 1.56(3) \times 10^{30}$  erg/s.

#### The ratio of X-ray and bolometric luminosities

It is well established that in late-type, solar-like stars, convection together with rotation gives rise to a magnetic dynamo operating at the base of the convective zone. The outcomes of this dynamo manifest themselves through magnetic phenomena in and above the stellar photosphere, such as starspots, magnetically confined coronal plasma, and episodic flaring activity. As expected, the level of X-ray emission correlates with the stellar rotation rate due to the rotation-driven internal dynamo. However, at the so-called canonical saturation threshold,  $L_X/L_{bol} \sim 10^{-3}$  (Vilhu, 1984; Wright et al., 2011; Freund et al., 2024), the X-ray luminosity ceases to increase with faster rotation. The physical origin of this saturation remains unclear. It may reflect an intrinsic limit of the dynamo itself or a near-complete filling of the stellar surface with magnetically active regions that dominate

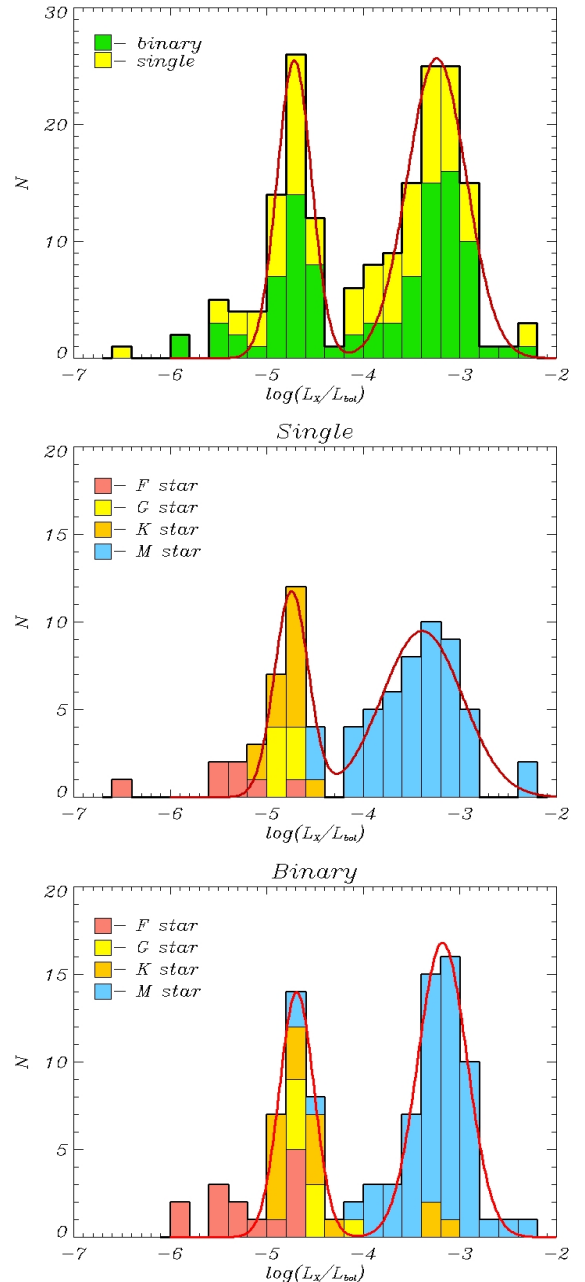


**Fig. 10.** Distribution of  $R_X = \log(L_X/L_{bol})$  for Hyades stars based on *e*ROSITA data. The red lines show a two-Gaussian fit. The lower- $R_X$  peak is formed primarily by FGK stars, while the higher- $R_X$  peak is populated by M stars. The distribution is shown as a stacked histogram, where each bin represents the sum of contributions from all color-coded subsamples. The middle panel shows the  $R_X$  distribution for single stars, and the bottom panel shows the distribution for stars with binarity.

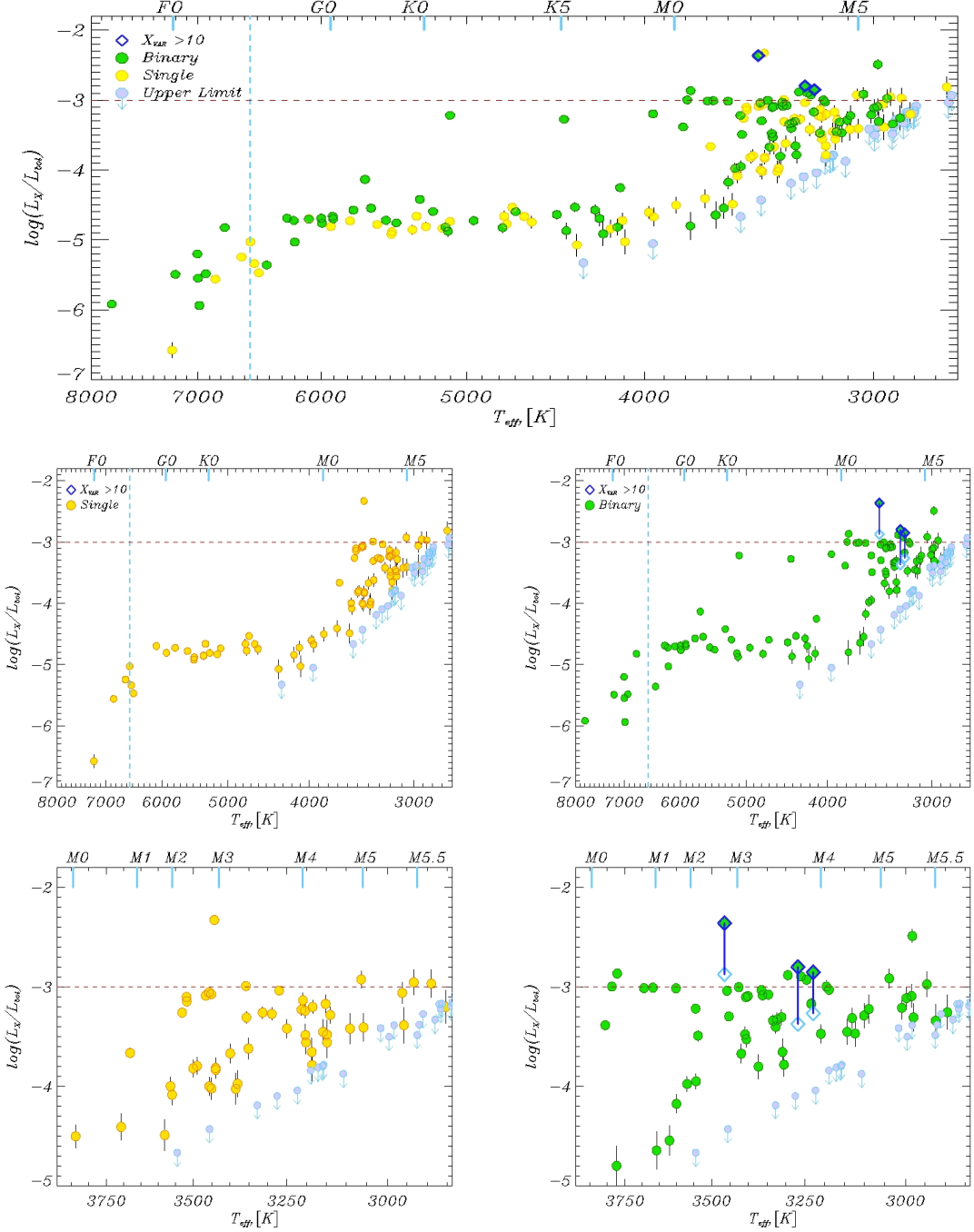


**Fig. 11.**  $\log(L_X/L_{\text{bol}})$  dependence on the effective temperature  $T_{\text{eff}}$  of the optical counterpart. The vertical dashed line marks the approximate boundary between stars with and without an outer convective envelope. The horizontal red dashed line indicates the canonical fractional X-ray luminosity level of  $10^{-3}$  of the bolometric luminosity. Stars with strong X-ray variability ( $X_{\text{var}} > 10$ ) are shown in blue. Sources with confirmed binarity are plotted in green. The top panel shows the full sample; the middle panel separates single and binary stars; the bottom panel reproduces the same separation but only for M-type stars (M0–M5.5).

**Table 4.** Parameters of the Gaussian fits to the bimodal distribution in  $R_X$ . The table lists the peak positions and the corresponding  $FWHM$  values in units of  $dex$ .

Sample	$max_1$	$FWHM_1$	$max_2$	$FWHM_2$
single	-4.74	0.4	-3.39	1.0
binary	-4.69	0.4	-3.18	0.6
all	-4.71	0.4	-3.24	0.7

the X-ray output (see, e.g., the review by Güdel & Nazé 2009).

The distribution of the quantity  $R_X = \log(L_X/L_{bol})$  is clearly bimodal (Fig. 10). The peak at lower  $R_X$  values is populated predominantly by FGK-type stars, while the second peak is formed mainly by M dwarfs, with only a few K-type binaries contributing to this higher-activity component. The bimodality is evident to a similar degree in both the multiplicity sample (lower panel) and in the single-star subsample (middle panel). Table 4 summarizes the results of the Gaussian fitting of the bimodal  $R_X$  distribution for stars without multiplicity (single), with multiplicity (binary), and for the entire sample (all).

A similar bimodality has been reported both for the Hyades and for the coeval Praesepe cluster ( $\sim 700$  Myr), including in the *ROSAT* data (Núñez et al., 2022). Bimodality has also been identified in the younger Pleiades cluster based on *eROSITA* observations (Khamitov et al., 2024). A bimodal  $R_X$  distribution is likewise seen among field stars (Freund et al., 2024), where coronally active stars within 1 kpc were identified using the first *eROSITA* all-sky survey on the western Galactic hemisphere. However, due to the sensitivity limitations as a function of distance, the lower- $R_X$  peak in the field-star sample is typically much less prominent than the higher-activity peak.

In the case of the Hyades, the observed bimodality cannot be corresponded to an incorrect determination of  $R_X$  in spectroscopic binaries, i.e. to situations where the bolometric luminosity is assigned to the more massive component while the X-ray emission is primarily produced by the lower-mass, coronally active secondary. The bimodality is of physical origin: the X-ray luminosities of sources forming the left peak, owing to the similarity of both the peak position and its width, do not depend on multiplicity and therefore reflect the intrinsic stellar properties, with more massive and larger stars exhibiting higher X-ray luminosities.

The dependence of  $R_X$  on stellar effective temperature is shown in Fig. 11. A clear trend is evident:  $R_X$  increases toward lower  $T_{\text{eff}}$ , with  $L_X/L_{bol}$  rising by more than three orders of magnitude from early- to

late-type stars. For single stars, a well-defined plateau is visible from late-F to late-K types, with a similar concentration of binary sources in the same region (middle panels). Approximately  $\sim 12\%$  of the objects exhibit  $R_X - 3$ , all of which are later than M0. All strongly variable X-ray sources ( $X_{\text{var}} \geq 10$ ), shown in blue in Fig. 11, also display  $R_X - 3$ , while correcting these strongly X-ray-variable sources to their quiescent state shifts them below this threshold (lower right panel, gray diamonds). M dwarfs, regardless of multiplicity, remain confined by the canonical upper limit of  $R_X < -3$  (lower panels). The only exception among single stars is the previously mentioned source SRGe J042829.0+174145, whose X-ray emission likely arises predominantly from a field BY Dra-type star.

To investigate the dependence of  $R_X$  on stellar rotation period ( $P$ ) and on the more robust indicator of coronal activity, the Rossby number<sup>2</sup> ( $Ro$ ), we compiled a unified catalog of rotation periods for Hyades members. Rotation information was gathered from publicly available data, incorporating measurements reported by Rutten (1987), Söderhjelm (1999), Debernardi et al. (2000), Isaacson & Fischer (2010), Cvetkovic & Ninkovic (2010), van Saders & Pinsonneault (2013), Newton et al. (2016), Rizzuto et al. (2017), Watson et al. (2017), Oelkers et al. (2018), Douglas et al. (2019), Lu et al. (2019), Freund et al. (2020), Muirhead et al. (2020), Chen et al. (2020), Bowler et al. (2020), Zhang et al. (2020), Battley et al. (2020), Popinchalk et al. (2021), Núñez et al. (2022), Prša et al. (2022), Tu et al. (2022), Gaia Collaboration (2022), Gaia Collaboration et al. (2023), Long et al. (2023), Gavras et al. (2023), Colman et al. (2024), Lu et al. (2024b), Lu et al. (2024a), Wang et al. (2024), and Qiao et al. (2024). We additionally used data from the *TESS* mission (Transiting Exoplanet Survey Satellite), which provides continuous, high-cadence photometric time series over long temporal baselines (Ricker et al., 2015). The rotation periods derived from *TESS* data and used in this study will be presented in Gorbachev et al. (2025, in press).

The convective turnover time ( $\tau$ ), required for estimating the Rossby number ( $Ro = P/\tau$ ), was evaluated using the empirical mass– $\tau$  relation from Wright et al. (2011). This relation is expressed as a second-order polynomial in log–log space:

$$\log(\tau) = 1.16 - 1.49\log(M/M_{\odot}) - 0.54\log^2(M/M_{\odot}) \quad (1)$$

This calibration is valid for stellar masses in the range  $0.09 < M/M_{\odot} < 1.36$ , i.e. for stars that possess an outer convective envelope. Our sample contains a small number of objects with  $M/M_{\odot} > 1.36$ , but since such stars lack a convective zone, the quantity  $\tau$

<sup>2</sup>[https://en.wikipedia.org/wiki/Rossby\\_number](https://en.wikipedia.org/wiki/Rossby_number)

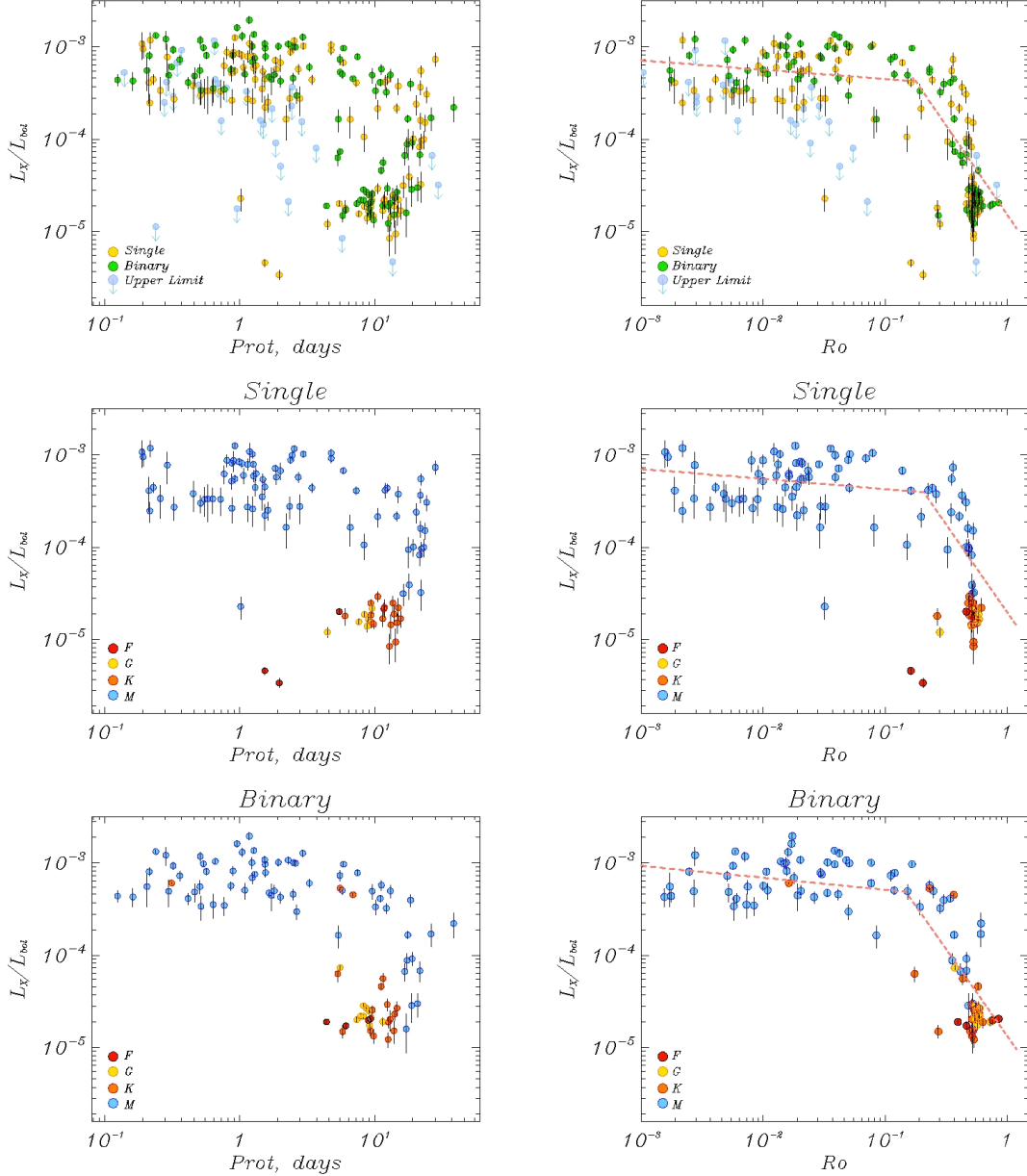


**Fig. 12.** Dependence of  $L_X/L_{\text{bol}}$  on stellar rotation period (left panels) and on Rossby number (right panels) for Hyades members. The top panels show the full sample, while the middle and bottom panels correspond to single and binary sources, respectively.

is not physically meaningful for them; they are therefore omitted from all Rossby-number analyses. We also exclude sources with  $X_{\text{var}} > 10$ , as their X-ray luminosities are likely overestimated due to being observed during flaring episodes. In addition, objects for which the 98% positional uncertainty circle ( $r_{98}$ ) contains more than one Hyades member from the 6d catalogue are removed from consideration.

The upper panels of Fig. 12 show the resulting relations between  $L_X/L_{\text{bol}}$  and the rotation period (left) and the Rossby number (right). Binary systems are indicated by green symbols, while sources without reliable evidence for multiplicity are shown in yellow.

The middle and lower panels present the same relations separately for the subsamples of single stars and systems with confirmed binarity. In these panels, individual spectral types are colour-coded to highlight their different loci in the  $P-R_X$  and  $Ro-R_X$  diagrams.

A pronounced dependence of  $R_X$  on  $Ro$  emerges at large Rossby numbers ( $Ro > 0.2$ ), where the data clearly show the transition from the saturated to the unsaturated coronal-activity regime above a critical  $Ro$  value. The saturated branch is populated almost exclusively by M dwarfs. To obtain a rough quantitative description of this behaviour, we modelled the relation with a broken power law, fitting M-type stars separately for the subsamples of single stars, binaries, and for the combined set of all M dwarfs. Because the intrinsic scatter of the data far exceeds the statistical uncertainties, we employed the geometric method for non-linear correlations with intrinsic dispersion (Piha-joki, 2017; Lanz et al., 2019) to estimate the model parameters and their confidence intervals. In addition, we applied a simple iterative outlier-rejection procedure, conceptually similar to a lightweight version of the RANSAC (Random Sample Consensus) algorithm, removing at each iteration a small fraction  $f$  of points with the largest orthogonal deviations from the model. Owing to the limited sample sizes, the number of iterations was kept to only 1–3. For this modelling we used a lightly modified version of the `orthogonal_regression`<sup>3</sup> IDL package.

The resulting broken-power-law fits are shown in Fig. 12 as dashed lines and are summarized in Table 5.

#### Exoplanets in the Hyades

Among the five known Hyades stars hosting exoplanets, three (HD 285507, K2-25, and K2-136) are detected in X-rays with *eROSITA*. For the remaining two systems no X-ray crossmatch was performed: TOI-4364 lies on the western Galactic hemisphere, and  $\epsilon$  Tau was excluded from our analysis based on the adopted *G*-band magnitude threshold. We note that

K2-136 is located beyond the tidal radius of the cluster, while K2-25 exhibits pronounced X-ray variability with  $X_{\text{var}} \sim 10$ . Table 6 lists the X-ray properties of Hyades planet-host stars derived from the *eROSITA* data in the 0.3–2.3 keV band.

#### CATALOG OF X-RAY BRIGHT STARS IN THE HYADES BASED ON *EROSITA* DATA BEYOND 3 TIDAL RADII

In the eastern Galactic tidal tail, we identified 114 X-ray emitting stars based on *eROSITA* observations in the 0.3–2.3 keV band. Within the  $r_{98}$  error circle of one X-ray source, two Hyades tidal tail stars are present, and the angular resolution of *eROSITA* is insufficient to unambiguously identify the optical counterpart. Apart from HD 213930, a red giant, all sources are main-sequence stars. The macroscopic parameters of these main-sequence stars were derived using the same methodology as applied for the sample within three tidal radii. A subset of the catalog of 113 *eROSITA* X-ray sources associated with Hyades stars beyond three tidal radii is provided in Table 7. The full catalog will also be made available electronically CDS.

Figure 13 presents the X-ray luminosity as a function of effective temperature for stars in the Hyades tidal tail, compared to stars located within three tidal radii of the cluster. Gray symbols indicate sources with distances from the cluster center  $r < 3r_{\text{tidal}}$ , while yellow symbols denote tidal tail sources with  $r > 3r_{\text{tidal}}$ .

In Figure 13, the red giant HD 213930 is highlighted with a blue star symbol. This source exhibits a substantial X-ray luminosity of  $L_X = 1.21 \times 10^{30} \text{ erg s}^{-1}$ , atypical for stars of this type; for comparison, deep *Chandra* exposures of the red giant Arcturus detected X-ray emission only at the level of  $3 \times 10^{25} \text{ erg s}^{-1}$  (Ayres, 2018). Within the  $r_{98}$  error circle, it is the only optical counterpart identified by *Gaia*. There is evidence for its binarity from detected anomalies in proper motion based on *Hipparcos* and *Gaia* DR2 measurements (Kervella et al., 2019). It is plausible that the X-ray emission originates from an M-type companion undergoing a flare. However, this X-ray source was observed in all five surveys and shows low X-ray variability ( $X_{\text{var}} \sim 2$ ). Additionally, the estimated mass of the secondary component is  $M_2 \approx 8.8 M_J$  (in Jupiter masses, assuming a 1 AU orbit), with a lower limit on the semimajor axis of 2.1 AU (Kervella et al., 2019).

Figure 13 also shows a notable deviation in X-ray luminosity for a tidal tail source around 6000 K (highlighted with a blue square). The only *Gaia* optical counterpart within the  $r_{98} \sim 9.2 \text{ arcsec}$  error circle is the binary system *HD 26090*, consisting of G0V and

<sup>3</sup>[https://github.com/lalanz/orthogonal\\_regression](https://github.com/lalanz/orthogonal_regression)

**Table 5.** Results of the orthogonal broken-line regression of the  $\log(Ro) - \log(L_X/L_{\text{bol}})$  relation. The columns are defined as follows:  $Ro_{\text{break}}$  — the Rossby number at the break point;  $C$ ,  $\text{err}(C)$  — normalization constant of the linear relation and its uncertainty in the saturated regime;  $\beta_1$ ,  $\text{err}(\beta_1)$  — power-law index and its uncertainty in the saturated regime;  $IS_1$ ,  $\text{err}(IS_1)$  — intrinsic scatter and its uncertainty in the saturated regime;  $\beta_2$ ,  $\text{err}(\beta_2)$  — power-law index and its uncertainty in the unsaturated regime;  $IS_2$ ,  $\text{err}(IS_2)$  — intrinsic scatter and its uncertainty in the unsaturated regime.

Type	$Ro_{\text{break}}$	$C$	$\text{err}(C)$	$\beta_1$	$\text{err}(\beta_1)$	$IS_1$	$\text{err}(IS_1)$	$\beta_2$	$\text{err}(\beta_2)$	$IS_2$	$\text{err}(IS_2)$
single	0.21	-3.48	0.09	-0.11	0.06	0.47	0.07	-1.90	0.27	0.33	0.10
binary	0.15	-3.42	0.12	-0.13	0.07	0.41	0.07	-1.88	0.20	0.28	0.11
all	0.18	-3.45	0.07	-0.10	0.04	0.45	0.05	-1.93	0.18	0.34	0.06

**Table 6.** X-ray luminosities of Hyades exoplanet host stars based on *eROSITA* data in the 0.3–2.3 keV energy band.

Name	SRGe+	$L_X$ ( $\times 10^{28}$ erg/s)	$X_{\text{var}}$	Reference		Note
HD285507	J040701.5+152005	1.6	4.0	Quinn et al. (2014)		
K2-25	J041305.7+151452	4.2	10.1	Mann et al. (2016)		
K2-136	J042938.9+225301	1.2	2.0	Mann et al. (2018)		
TOI-4364				Distler et al. (2025)	western hemisphere	
$\epsilon$ Tau				Sato et al. (2007)	excluded by $G$	

**Table 7.** *eROSITA* X-ray sources associated with Hyades stars in the eastern Galactic tidal tail.

SRGe+	Gaia DR3+	RA ( $^{\circ}$ )	DEC ( $^{\circ}$ )	G (mag)	$r_{98}$ (")	sep (")	N	$L_X$	$L_X.\text{err}$	$\log \frac{L_X}{L_{\text{bol}}}$ (dex)	$X_{\text{var}}$	$SpT$
J000237.2+515643	395696646953688448	0.65351	51.9453	10.8	6.8	3.7	2	1.24	0.25	-4.69	> 4.0	K6V
J000552.3+630914	431526153186969856	1.47071	63.1534	12.0	7.1	5.0	3	1.04	0.24	-4.47	> 2.0	K9V
J000852.5+531247	396026569162536448	2.22044	53.2133	10.0	6.3	3.8	1	3.52	0.67	-4.85	> 2.0	G9V
J001257.8+505917	395368374014574848	3.24106	50.9883	14.8	5.0	1.3	1	0.73	0.10	-3.29	2.3	M5V
J002200.0+473107	392484114490982656	5.49985	47.5178	14.1	5.0	2.4	2	2.34	0.43	-3.53	> 4.1	M3V
J002342.1+505124	394745294513036800	5.92421	50.8570	15.7	8.7	3.0	1	0.50	0.14	-3.42	> 3.2	M5V
J002652.2+425003	382167740483722112	6.71791	42.8341	11.9	2.5	0.7	1	10.7	0.51	-3.14	> 1.9	M1.5V
J003353.7+554544	418631085120675840	8.47192	55.7626	16.0	7.1	4.3	2	1.37	0.35	-3.22	> 3.1	M4.5V

\* Several Pleiades stars are located within the  $r_{98}$  positional uncertainty circle of the X-ray source.

The full table is available in the archive of the Strasbourg Astronomical Data Center (CDS). Columns are defined as follows: (1) source identification number in the *SRG/eROSITA* catalog; (2–5) Gaia DR3 identifier, right ascension and declination in degrees (J2000.0), and the *G*-band magnitude; (6)  $r_{98}$  — the 98% positional uncertainty radius of the *eROSITA* source (arcsec); (7) angular separation between the X-ray and optical positions (arcsec); (8)  $N$  — the number of Gaia DR3 optical sources within  $r_{98}$ ; (9) X-ray luminosity estimate from the five *eROSITA* all-sky surveys in the 0.3–2.3 keV band, in units of  $\times 10^{28}$  erg s $^{-1}$ ; (10) associated uncertainty of the X-ray luminosity, in units of  $\times 10^{28}$  erg s $^{-1}$ ; (11) logarithm of the ratio  $L_X/L_{\text{bol}}$  derived from the five *eROSITA* surveys in the 0.3–2.3 keV band; (12)  $X_{\text{var}}$  — the X-ray variability factor, defined as the ratio of maximum to minimum flux measured across the five *eROSITA* surveys; (13)  $SpT$  — spectral class of the star.

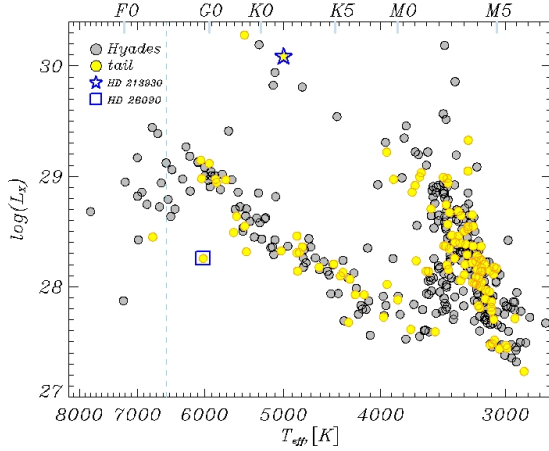


**Fig. 13.** Distribution of X-ray luminosity ( $L_X$ ) as a function of effective temperature ( $T_{\text{eff}}$ ) for X-ray-detected stars in the eastern tidal tail based on *eROSITA* data.

G5V components (Stephenson & Sanwal, 1969). The surrounding sky region was scanned by the *SRG* observatory in four surveys. The source was detected in only one survey at  $F_X = 5.2 \times 10^{-14}$  erg s $^{-1}$  cm $^{-2}$ , while in the other three surveys it was undetected with upper limits of  $F_X \sim 2 \times 10^{-14}$  erg s $^{-1}$  cm $^{-2}$ , yielding  $X_{\text{var}} \sim 2.6$ . Such variability is unusual for G-type stars in our 6d sample, which were detected in all surveys with  $X_{\text{var}}$  not exceeding a factor of 2. The expected X-ray luminosity for a G0 star assuming 100% detection within the tidal radius is  $\sim 10^{29}$  erg s $^{-1}$ , i.e., an order of magnitude higher. These considerations strongly suggest that *HD 26090* is likely not a member of the Hyades.

#### COMPARISON WITH THE *ROSAT* DATA

More than three decades ago, the Hyades region was observed with the *ROSAT* satellite. These observations enabled the identification of point sources with optical Hyades members (Pye et al. (1994); Stern et al. (1995)). The availability of high-precision astrometric data from *Gaia* has since refined the cluster membership. Freund et al. (2020) and later Núñez et al. (2022) revisited the *ROSAT* source identifications using updated *Gaia* data. A comparison between the *ROSAT* and *eROSITA* catalogs allows us to characterize the long-term X-ray variability of Hyades stars on a  $\sim 30$ -year timescale.

We cross-matched the *eROSITA* sources with *ROSAT* data from the *J/ApJ/931/45* catalog, which provides X-ray fluxes in the 0.1–2.4 keV band. To account for the varying positional uncertainties of *ROSAT* sources, we considered three distinct regions of the *ROSAT* field of view, depending on the off-axis

angle. Following the approach of Micela et al. (1996), matches were searched within circular regions of  $30''$ ,  $60''$ , and  $120''$  for the central ( $\theta \leq 20'$ ), intermediate ( $20' < \theta \leq 30'$ ), and outer ( $30' < \theta \leq 50'$ ) zones, respectively. For reference, the localization accuracy of *eROSITA* sources is much higher, with typical  $r98$  values not exceeding  $\sim 10''$ . In total, 108 matches between the two catalogs were found. In nine cases, two *eROSITA* sources were found within a single *ROSAT* error circle; such *ROSAT* sources were excluded from the 30-year variability analysis.

Table 8 lists the matches between *ROSAT* and *eROSITA* sources. Comparison of the *ROSAT* and *eROSITA* catalogs allows us to characterize the long-term ( $\sim 30$  yr) X-ray variability of Hyades stars. For this analysis, we use the variability factor  $X_{\text{var}}$ . Only *eROSITA* sources with a single counterpart within the *ROSAT* error circle were considered. For each source,  $X_{\text{var}}$  was computed as the ratio of the higher to the lower X-ray luminosity between  $L_{X,\text{ROSAT}}$  and  $L_{X,\text{eROSITA}}$ . Figure 14 shows  $X_{\text{var}}$  as a function of stellar effective temperature. Several late-type stars exhibit variability of up to  $\sim 10$  times, while most sources show moderate changes, with flux variations up to  $\sim 2$ – $3$  over 30 yr. Notably, sources that are highly variable over the 2-year *eROSITA* survey often do not display strong long-term variability. This is further illustrated in Fig. 15, showing the correlation between 2-year  $X_{\text{var}}$  from *eROSITA* and 30-year  $X_{\text{var}}$ . Sources with only lower limits on 2-year variability are plotted in gray, and the red dashed line indicates  $R = 1$ . The figure demonstrates that, for most sources, short-term variability (2 yr) exceeds long-term variability (30 yr). Stars strongly variable on 2-year timescales do not necessarily exhibit strong variability over 30 yr, whereas stars with high 30-year variability only provide lower limits on their 2-year variability. It should be noted that the estimation of X-ray fluxes from both *eROSITA* and *ROSAT* is model-dependent, and the associated uncertainty may reach several tens of percent. This circumstance naturally introduces some uncertainty in the evaluation of  $X_{\text{var}}$  on a 30-year timescale, but it remains within the error margins and does not significantly affect the conclusions regarding variability. When interpreting this correlation, flare activity can contribute significantly to the 2-year variability. Further analysis will be presented in future publications.

#### CONCLUSION

The region surrounding the Hyades open cluster was observed with the *eROSITA* X-ray telescope aboard the *SRG* observatory, partially in four and partially in five all-sky surveys. As a result, in the 0.3–2.3 keV band a flux sensitivity of  $F_{X,0.3-2.3} \sim$

**Table 8.** List of matches between *eROSITA* and *ROSAT* sources in the Hyades.

SRGe+	Instr	Source	RA ( $^{\circ}$ )	DEC ( $^{\circ}$ )	$\Delta$ ( $''$ )	off-axis ( $'$ )	$F_X$	$eF_X$	$F_{X,ero}$	$eF_{X,ero}$	$N_{ero}$	$N_{gaia}$
J040045.1+135423	PSPC	2RXS	60.1846619	13.9069004	11.2		4.1	11.2	2.5	1.8	1	1
J035453.3+161856	PSPC	2RXS	58.7233086	16.3204994	18.5		8.7	15.0	15.9	4.8	1	1
J035506.6+165955	PSPC	2RXS	58.7753716	17.0031300	17.7		2.6	8.7	1.1	1.2	1	1
J035310.2+171936	PSPC	2RXP	58.2913017	17.3297005	11.7	20	4.6	1.7	3.0	2.0	1	1
J035025.1+171447	PSPC	2RXP	57.6016998	17.2474995	10.4	1	99.5	13.6	32.2	6.6	1	1
J040742.0+150945	PSPC	2RXS	61.9269295	15.1575603	18.8		2.8	11.1	3.1	2.0	1	2
J040701.5+152005	PSPC	S01	61.7649994	15.3361111	31.4	24	0.5	3.0	0.7	1.0	1	1
J040616.3+154154	PSPC	2RXP	61.5691986	15.6989002	5.0	1	4.7	6.4	3.0	2.0	1	1
J041613.7+164751	PSPC	2RXP	64.0553970	16.7964001	7.4	13	0.3	0.4	0.3	0.8	1	1
J041739.1+165652	HRI	1RXH	64.4115982	16.9498005	8.2	1	14.6	12.1	9.9	4.3	2	1

The full table is available in the Strasbourg Astronomical Data Center archive. The columns are defined as follows:  
1) Source identifier in the *SRG/eROSITA* catalog; 2) ROSAT instrument; 3) X-ray data source; 4) angular separation between the *ROSAT* and *eROSITA* sources; 5–6) right ascension and declination of the ROSAT source (J2000.0); 7) off-axis angle of the ROSAT X-ray source in arcminutes; 8) ROSAT X-ray flux in the 0.1–2.4 keV band, in units of  $\times 10^{-13}$  erg s $^{-1}$  cm $^{-2}$ ; 9) flux uncertainty from ROSAT in the same band; 10) *eROSITA* X-ray flux in the 0.3–2.3 keV band, in units of  $\times 10^{-13}$  erg s $^{-1}$  cm $^{-2}$ ; 11) flux uncertainty from *eROSITA* in the same band; 12)  $N_{ero}$  – number of *eROSITA* sources in the Hyades within the ROSAT positional error circle previously associated with a cluster star; 13)  $N_{gaia}$  – number of optical Hyades sources from the 6d catalog based on *Gaia DR3* within the r98 error circle of the *eROSITA* source. X-ray data source identifiers (Source) follow Núñez et al. (2022): 2RXS = 2nd ROSAT all-sky survey, Boller et al. (2016), *J/A+A/588/A103*; 2RXP = Second ROSAT PSPC Catalog, *IX/30*; S01 = Stelzer & Neuhäuser (2001); S95 = Stern et al. (1995), *J/ApJ/448/683*; 1RXH = ROSAT HRI pointed observations, Cat. *IX/28*.

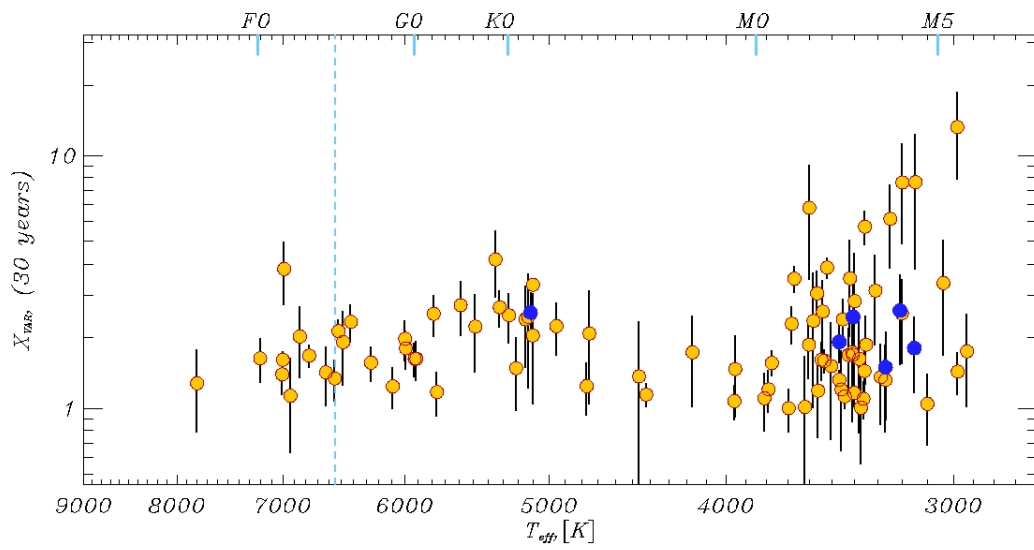


**Fig. 14.** X-ray variability of Hyades sources over a 30-year timescale from *ROSAT* and *eROSITA* as a function of stellar  $T_{eff}$ . Blue symbols indicate sources with short-term variability (based on 4–5 *eROSITA* surveys, i.e.,  $\sim 1.5$ –2 yr) exceeding a factor of 5.

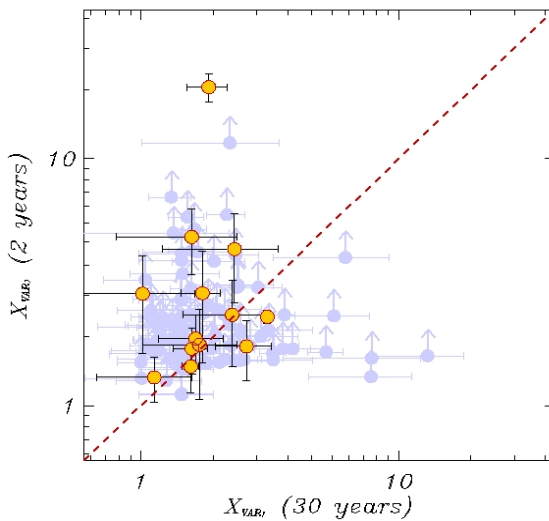


**Fig. 15.** Relation between  $X_{var}$  on a 2-year timescale from *eROSITA* and on a 30-year timescale.

$1.1 \times 10^{-14} \text{ erg s}^{-1} \text{ cm}^{-2}$  (median value) was reached, corresponding at the Hyades distance (47 pc) to an X-ray luminosity of  $L_{X,0.3-2.3} \sim 2.6 \times 10^{27} \text{ erg s}^{-1}$ . In total, 290 *eROSITA* X-ray sources were associated with cluster members in the eastern Galactic hemisphere, of which 171 were detected in X-rays for the first time. Optical identifications were performed using a Hyades star catalog based on *Gaia DR3* (Žerjal et al., 2023), with 15 cases where the 98% positional error circle included two Hyades stars. The *eROSITA* detection fraction reached  $\sim 83\%$  within the cluster tidal radius and  $\sim 70\%$  beyond it, yielding an overall detection rate of  $\sim 77\%$  for the entire Hyades sample studied here, and an absolute 100% detection fraction for F0–K5 stars inside the tidal radius.

X-ray emitting stars are detected across all spectral types, from late-A to late-M dwarfs (M9V). Considering that the X-ray luminosity of A-type stars (Drake et al., 2014; Günther et al., 2022) is several orders of magnitude below the survey sensitivity achieved by *eROSITA* at the Hyades distance, the observed X-ray emission of A stars is most likely due to the presence of a cooler secondary in a binary system. The *eROSITA* sources associated with Hyades members emit a total X-ray luminosity of  $L_{X,\text{total}} \sim 1.8 \times 10^{31} \text{ erg s}^{-1}$  (or  $\sim 4 \times 10^{31} \text{ erg s}^{-1}$  for the entire cluster). The highest X-ray luminosity is observed for the dK0 star  $L_{X,0.3-2.3} \sim 1.6 \times 10^{30} \text{ erg s}^{-1}$ , the RS CVn-type spectroscopic binary V1313 Tau, which alone contributes 10% of the total measured sample.

For six sources, the *eROSITA* detectors recorded strong X-ray variability between scans, with the ra-

tio of maximum to minimum flux exceeding a factor of 10. Three of these sources lie within the cluster's tidal radius and belong to the dM spectral type. No peculiarities are reported for these stars in the literature. The observed high flux variability is most likely caused by stellar flares occurring during one of the all-sky surveys. A dedicated study of stellar flares in the Hyades will be presented in a separate publication.

The logarithm of the X-ray to bolometric luminosity ratio for Hyades stars,  $R_X = \log(L_X/L_{bol})$ , increases from  $-7$  to  $-2$  with decreasing stellar effective temperature. The distribution of stars in  $R_X$  is bimodal, with peaks around  $R_X \sim -4.7$  and  $R_X \sim -3.2$ . The left peak at lower  $R_X$  is dominated by FGK stars with a minor contribution from M dwarfs, while the right peak at  $R_X \sim -3.2$  is mainly populated by M-type stars.

The dependence of  $R_X$  on the Rossby number exhibits a complex behavior that varies across spectral types. FGK stars, with a few exceptions in binary systems, are clustered at high Rossby numbers,  $Ro \sim 0.6$ – $0.8$ , with low  $R_X \sim -4.7$ . The relation for M dwarfs can be described by a broken power law: at low  $Ro$ ,  $R_X$  shows little dependence on  $Ro$ , whereas above a threshold of  $Ro \sim 0.2$ ,  $R_X$  increases sharply. This behavior can be interpreted as saturation of coronal activity at low Rossby numbers and has been reported in previous studies (Vilhu (1984), Wright et al. (2011), Freund et al. (2024)). M dwarfs also exhibit a significant scatter in  $R_X$  of about 0.4 dex. The  $Ro$ – $R_X$  relation for F-type stars appears more scattered; however, our sample is too limited for a detailed characterization of F-star behavior.

X-ray emission is detected by *eROSITA* for three Hyades stars hosting exoplanets in the eastern Galactic hemisphere (HD 285507, K2-25, and K2-136). The system hosting  $\epsilon$  Tau was not studied due to its low apparent magnitude in the  $G$  band, where *eROSITA* data are unreliable. Notably, the host star of K2-25 exhibits strong X-ray variability,  $X_{var} \sim 10$ , which likely has a significant impact on the physical environment of its exoplanet.

A comparison with the *ROSAT* catalog was carried out within the cluster's tidal radius. In the studied region, 108 matches between *eROSITA* and *ROSAT* sources were found. In 9 cases, two *eROSITA* sources fall within the *ROSAT* positional error circle. We compared the X-ray variability of the sources on timescales of 30 years and 2 years.

This work is based on observations with the *eROSITA* telescope onboard the SRG observatory. The SRG observatory was built by Roscosmos in the interests of the Russian Academy of Sciences represented by its Space Research Institute (IKI) within

the framework of the Russian Federal Space Program, with the participation of the Deutsches Zentrum fuer Luft- und Raumfahrt (DLR). The SRG/eROSITA X-ray telescope was built by a consortium of German Institutes led by MPE, and supported by DLR. The SRG spacecraft was designed, built, launched, and is operated by the Lavochkin Association and its subcontractors. The science data are downlinked via the Deep Space Network Antennae in Bear Lakes, Ussurijsk, and Baykonur, funded by Roskosmos. The eROSITA data used in this work were processed using the eSASS software system developed by the German eROSITA consortium and the proprietary data reduction and analysis software developed by the Russian eROSITA Consortium. This research has made use of the SIMBAD database, operated at CDS, Strasbourg, France.

The study was supported by a grant from the Russian Science Foundation N 23-12-00292.

## REFERENCES

1. T. R. Ayres, Astron. J., **156**, 163 (2018)
2. M. P. Battley, D. Pollacco, and D. J. Armstrong, Mon. Not. R. Astron. Soc., **496**, 1197 (2020)
3. T. Boller, M. J. Freyberg, J. Trümper, F. Haberl, W. Voges, and K. Nandra, Astron. Astrophys., **588**, A103 (2016)
4. B. P. Bowler, S. C. Blunt, and E. L. Nielsen, Astron. J., **159**, 63 (2020)
5. W. Brandner, P. Calissendorff, and T. Kopytova, Astron. Astrophys., **677**, A162 (2023)
6. A. Bressan, P. Marigo, L. Girardi, B. Salasnich, C. Dal Cero, S. Rubele, et al., Mon. Not. R. Astron. Soc., **427**, 127 (2012)
7. X. Chen, S. Wang, L. Deng, R. de Grijs, M. Yang, and H. Tian, Astrophys. J. Suppl. Ser., **249**, 18 (2020)
8. I. L. Colman, R. Angus, T. David, J. Curtis, S. Hattori, and Y. L. Lu, Astron. J., **167**, 189 (2024)
9. Z. Cvetkovic and S. Ninkovic, Serbian Astronomical Journal, **180**, 71 (2010)
10. Y. Debernardi, J. C. Mermilliod, J. M. Carquillat, and N. Ginestet, Astron. Astrophys., **354**, 881 (2000)
11. A. Distler, M. Soares-Furtado, A. Vanderburg, J. Schulte, J. Becker, A. W. Mann, et al., Astron. J., **169**, 166 (2025)
12. S. T. Douglas, J. L. Curtis, M. A. Agüeros, P. A. Cargile, J. M. Brewer, S. Meibom, et al., Astrophys. J., **879**, 100 (2019)
13. J. J. Drake, J. Braithwaite, V. Kashyap, H. M. Günther, and N. J. Wright, Astrophys. J., **786**, 136 (2014)
14. S. Freund, J. Robrade, P. C. Schneider, and J. H. M. M. Schmitt, Astron. Astrophys., **640**, A66 (2020)
15. S. Freund, S. Czesla, P. Predehl, J. Robrade, M. Salvato, P. C. Schneider, et al., Astron. Astrophys., **684**, A121 (2024)
16. Gaia Collaboration, A. Vallenari, A. G. A. Brown, T. Prusti, J. H. J. de Bruijne, F. Arenou, et al., Astron. Astrophys., **674**, A1 (2023)
17. Gaia Collaboration, *VizieR Online Data Catalog: Gaia DR3 Part 4. Variability (Gaia Collaboration, 2022)*, VizieR On-line Data Catalog: I/358. Originally published in: 2023A&A...674A...1G (2022)
18. P. Gavras, L. Rimoldini, K. Nienartowicz, G. J. de Fombelle, B. Holl, P. Ábrahám, et al., Astron. Astrophys., **674**, A22 (2023)
19. R. Gratton, M. Bonavita, D. Mesa, S. Desidera, A. Zurlo, S. Marino, et al., Astron. Astrophys., **694**, A175 (2025)
20. M. Güdel and Y. Nazé, , **17**, 309 (2009)
21. H. M. Günther, C. Melis, J. Robrade, P. C. Schneider, S. J. Wolk, and R. K. Yadav, Astron. J., **164**, 8 (2022)
22. G. A. J. Hussain, C. Allende Prieto, S. H. Saar, and M. Still, Mon. Not. R. Astron. Soc., **367**, 1699 (2006)
23. H. Isaacson and D. Fischer, Astrophys. J., **725**, 875 (2010)
24. T. Jerabkova, H. M. J. Boffin, G. Beccari, G. de Marchi, J. H. J. de Bruijne, and T. Prusti, Astron. Astrophys., **647**, A137 (2021)
25. P. Kervella, F. Arenou, F. Mignard, and F. Thévenin, Astron. Astrophys., **623**, A72 (2019)
26. I. M. Khamitov, I. F. Bikmaev, M. R. Gilfanov, R. A. Sunyaev, and P. S. Medvedev, Astronomy Letters, **50**, 780 (2024)
27. L. Lanz, R. C. Hickox, M. Baloković, T. Shimizu, C. Ricci, A. D. Goulding, et al., Astrophys. J., **870**, 26 (2019)
28. N. Lodieu, R. L. Smart, A. Pérez-Garrido, and R. Silvotti, Astron. Astrophys., **623**, A35 (2019)
29. L. Long, S. Bi, J. Zhang, X. Zhang, L. Zhang, Z. Ge, et al., Astrophys. J. Suppl. Ser., **268**, 30 (2023)
30. H.-p. Lu, L.-y. Zhang, J. Shi, X. L. Han, D. Fan, L. Long, et al., Astrophys. J. Suppl. Ser., **243**, 28 (2019)
31. Y. Lu, R. Angus, D. Foreman-Mackey, and S. Hattori, Astron. J., **167**, 159 (2024a)
32. Y. L. Lu, V. See, L. Amard, R. Angus, and S. P. Matt, Nature Astronomy, **8**, 223 (2024b)
33. A. W. Mann, E. Gaidos, G. N. Mace, M. C. Johnson, B. P. Bowler, D. LaCourse, et al., Astrophys. J., **818**, 46 (2016)
34. A. W. Mann, A. Vanderburg, A. C. Rizzuto, A. L. Kraus, P. Berlind, A. Bieryla, et al., Astron. J., **155**, 4 (2018)
35. S. Meingast and J. Alves, Astron. Astrophys., **621**, L3 (2019)
36. G. Micela, S. Sciortino, G. S. Vaiana, J. H. M. M. Schmitt, R. A. Stern, F. R. Harnden, Jr., et al., Astrophys. J., **325**, 798 (1988)
37. G. Micela, S. Sciortino, V. Kashyap, J. Harnden, F. R., and R. Rosner, Astrophys. J. Suppl. Ser., **102**, 75 (1996)

38. P. S. Muirhead, M. J. Veyette, E. R. Newton, C. A. Theissen, and A. W. Mann, *Astron. J.*, **159**, 52 (2020)
39. P. S. Muirhead, J. Nordhaus, and M. R. Drout, *Astron. J.*, **163**, 34 (2022)
40. M. Netopil, E. Paunzen, U. Heiter, and C. Soubiran, *Astron. Astrophys.*, **585**, A150 (2016)
41. E. R. Newton, J. Irwin, D. Charbonneau, Z. K. Berta-Thompson, J. A. Dittmann, and A. A. West, *Astrophys. J.*, **821**, 93 (2016)
42. A. Núñez, M. A. Agüeros, K. R. Covey, S. T. Douglas, J. J. Drake, R. Rampalli, et al., *Astrophys. J.*, **931**, 45 (2022)
43. R. J. Oelkers, J. E. Rodriguez, K. G. Stassun, J. Pepper, G. Somers, S. Kafka, et al., *Astron. J.*, **155**, 39 (2018)
44. (S. S. R. Offner, M. Moe, K. M. Kratter, S. I. Sadavoy, E. L. N. Jensen, and J. J. Tobin), in S. Inutsuka, Y. Aikawa, T. Muto, K. Tomida, and M. Tamura (eds.), *Protostars and Planets VII*, Vol. 534 of Astronomical Society of the Pacific Conference Series, p. 275 (2023)
45. M. J. Pecaut and E. E. Mamajek, *Astrophys. J. Suppl. Ser.*, **208**, 9 (2013)
46. P. Pihajoki, *Mon. Not. R. Astron. Soc.*, **472**, 3407 (2017)
47. M. Popinchalk, J. K. Faherty, R. Kiman, J. Gagné, J. L. Curtis, R. Angus, et al., *Astrophys. J.*, **916**, 77 (2021)
48. P. Predehl, R. Andritschke, V. Arefiev, V. Babyshkin, O. Batanov, W. Becker, et al., *Astron. Astrophys.*, **647**, A1, 16 (2021)
49. A. Prša, A. Kochoska, K. E. Conroy, N. Eisner, D. R. Hey, L. IJspeert, et al., *Astrophys. J. Suppl. Ser.*, **258**, 16 (2022)
50. J. P. Pye, S. T. Hodgkin, R. A. Stern, and J. R. Stauffer, *Mon. Not. R. Astron. Soc.*, **266**, 798 (1994)
51. P. Qiao, T. Xu, F. Wang, Y. Mei, H. Deng, L. Tan, et al., *Astrophys. J. Suppl. Ser.*, **272**, 1 (2024)
52. S. N. Quinn, R. J. White, D. W. Latham, L. A. Buchhave, G. Torres, R. P. Stefanik, et al., *Astrophys. J.*, **787**, 27 (2014)
53. G. R. Ricker, J. N. Winn, R. Vanderspek, D. W. Latham, G. Á. Bakos, J. L. Bean, et al., *Journal of Astronomical Telescopes, Instruments, and Systems*, **1**, 014003 (2015)
54. A. C. Rizzuto, A. W. Mann, A. Vanderburg, A. L. Kraus, and K. R. Covey, *Astron. J.*, **154**, 224 (2017)
55. S. Röser, E. Schilbach, and B. Goldman, *Astron. Astrophys.*, **621**, L2 (2019)
56. R. G. M. Rutten, *Astron. Astrophys.*, **177**, 131 (1987)
57. N. N. Samus', E. V. Kazarovets, O. V. Durlevich, N. N. Kireeva, and E. N. Pastukhova, *Astronomy Reports*, **61**, 80 (2017)
58. B. Sato, H. Izumiura, E. Toyota, E. Kambe, Y. Takeda, S. Masuda, et al., *Astrophys. J.*, **661**, 527 (2007)
59. V. V. Shimansky, I. F. Bikmaev, and N. N. Shimanskaya, *Astrophysical Bulletin*, **66**, 449 (2011)
60. S. Söderhjelm, *Astron. Astrophys.*, **341**, 121 (1999)
61. B. Stelzer and R. Neuhäuser, *Astron. Astrophys.*, **377**, 538 (2001)
62. C. B. Stephenson and N. B. Sanwal, *Astron. J.*, **74**, 689 (1969)
63. R. A. Stern, M. C. Zolcinski, S. K. Antiochos, and J. H. Underwood, *Astrophys. J.*, **249**, 647 (1981)
64. R. A. Stern, J. H. M. M. Schmitt, and P. T. Kahabka, *Astrophys. J.*, **448**, 683 (1995)
65. R. Sunyaev, V. Arefiev, V. Babyshkin, A. Bogomolov, K. Borisov, M. Buntov, et al., *Astron. Astrophys.*, **656**, A132, 29 (2021)
66. S. Torniamenti, M. Gieles, Z. Penoyre, T. Jerabkova, L. Wang, and F. Anders, *Mon. Not. R. Astron. Soc.*, **524**, 1965 (2023)
67. G. Torres, G. H. Schaefer, R. P. Stefanik, D. W. Latham, A. F. Boden, N. Anugu, et al., *Astrophys. J.*, **971**, 31 (2024)
68. Z.-L. Tu, Q. Wu, W. Wang, G. Q. Zhang, Z.-K. Liu, and F. Y. Wang, *Astrophys. J.*, **935**, 90 (2022)
69. J. L. van Saders and M. H. Pinsonneault, *Astrophys. J.*, **776**, 67 (2013)
70. O. Vilhu, *Astron. Astrophys.*, **133**, 117 (1984)
71. M. Žerjal, N. Lodieu, A. Pérez-Garrido, J. Olivares, V. J. S. Béjar, and E. L. Martín, *Astron. Astrophys.*, **678**, A75 (2023)
72. Y. Wang, L. Zhang, T. Su, X. L. Han, and P. Misra, *Astron. Astrophys.*, **686**, A164 (2024)
73. C. Watson, A. A. Henden, and A. Price, *VizieR Online Data Catalog: AAVSO International Variable Star Index VSX (Watson+, 2006-2014)*, VizieR Online Data Catalog: B/vsx. Originally published in: 2006SASS...25...47W (2017)
74. N. J. Wright, J. J. Drake, E. E. Mamajek, and G. W. Henry, *Astrophys. J.*, **743**, 48 (2011)
75. L.-Y. Zhang, L. Long, J. Shi, H.-P. Lu, Q. Gao, X. L. Han, et al., *Mon. Not. R. Astron. Soc.*, **495**, 1252 (2020)